On-demand switchable superamphiphilic nanofiber membrane reinforced by PET braided tube for efficient wastewater purification and photocatalytic regeneration

Hongwei Piao [a,1], Jian Zhao [a,*,1], Yifei Tang [b], Run Zhang [a], Shujie Zhang [a], Qinglin Huang [b,*], Shiwei Zuo [c], Yong Liu [a], Changfa Xiao [d], Shaomin Liu [a,e,**]

[a] State Key Laboratory of Separation Membranes and Membrane Processes, School of Textile Science and Engineering, Tiangong University, Tianjin 300387, China
[b] National Center for International Joint Research on Separation Membranes, School of Material Science and Engineering, Tiangong University, Tianjin 300387, China
[c] Sinopec Engineering Group Luoyang R&D Center of Technologies, China
[d] Fiber Materials Research Center, Shanghai University of Engineering Science, Shanghai 201620, China
[e] WA School of Mines: Minerals, Energy and Chemical Engineering, Curtin University, Perth, WA 6102 Australia

A B S T R A C T

Nanofiber membrane is regarded as one of the ideal candidates for complex wastewater purification. However, the membrane fragility, fouling and dull wettability limits its widespread application. In this work, a hybrid zeolitic imidazolate framework-8 @zinc oxide nanorod decorated poly (vinylidene fluoride) tubular nanofiber membrane (ZIF-8 @ZnO/PVDF-TNM) was developed based on a polyester braided tubular reinforcement substrate. The hybrid membrane was fabricated by ZnO seeds conversion, ZnO nanowire growth via hydrothermal technique and ZIF-8 deposition using self-template scarifying method. The resultant ZIF-8 @ZnO/PVDF-TNM possesses enhanced photocatalytic capacity for pollutants removal and superamphiphilicity or under-liquid superamphiphobicity depending on its nanoarchitecture. In virtue of well-grown ZIF-8 @ZnO nanorods, the membrane exhibits a commendable permeation ability (784 and 865 $L \cdot m^{-2} \cdot h^{-1}$ for water and oil, respectively) under gravity operation, superior oil/water separation efficiency ($> 99.9\%$) for various emulsions. Moreover, it can achieve high-efficient pollutants degradation, self-cleaning and membrane regeneration by solar light irradiation. This study demonstrates a new approach to fabricate the switchable superamphiphilic nanofiber membrane for water remediation and membrane regeneration.

1. Introduction

With the proceeding of industrial civilization, environmental problems have hindered the sustainable development of human society over the past decades. The arbitrary discharge of industrial and domestic wastewater has produced tremendous concerns on the ecological environment and fresh water, causing an irreversible shortage of clean water resources [1,2]. Usually, industrial wastewater is a typically complex mixture containing various oils, organic solvents, textile dyes, surfactants, hazardous substance and other pollutants [3,4]. Such complex oily wastewater, is easily precipitated or transformed to other carcinogenic

substances, causing a huge challenge in the nature for the subsequent conversion into environmentally benign chemicals [5]. Therefore, the purification of the wastewater containing toxic chemicals exceeding the natural remediation capacity has become an important issue that should be solved urgently [6–9].

Nanofiber membranes have attracted extensive attention in the field of water purification due to its high porosity, excellent permeability, and tunable functionality [10,11]. Currently, many studies on remediation of various complex oily wastewater with nanofiber membranes have been reported [12–15]. The numerous nanofiber membranes as reported show a high separation efficiency for treating oil-in-water emulsions or

---

water-in-oil emulsions; however, their mechanical ability, operational stability and antifouling performance need a further improvement [16–18]. Moreover, the oil/water filtration membrane with inflexible wettability cannot meet the current requirement to process complex oily wastewater [19,20]. Based on classic Young's equation, water contact angle (WCA) and oil contact angle (OCA) on a given membrane surface are conventionally supplementary to each other, which means that the same surface is always expected to show a hydrophilic/underwater oleophobic or hydrophobic/underoil hydrophobic ability. Therefore, the special dual lyophobic state may be catered to some harsh conditions. Recently, such special or switchable wettability of membranes is mainly achieved via several feasible methods to control temperature, UV-light illumination, pH, voltage and so on. Particularly, during the long-term filtration with contaminants being accumulated, the ideal selective wettability of membrane surface gradually disappeared, lowering the separation capability [21–24]. In addition, the ordinary oil/water separation nanofiber membrane is easily contaminated by various pollutants and physically damaged by external forces, which dramatically reduces the membrane life [25,26]. On consideration of the research gaps, advanced oxidation process (AOP) has been coordinated with filtration membrane to construct a multifunctional catalytic membrane in order to realize the "catalysis+ separation" simultaneously and overcome the severe membrane fouling for complex wastewater remediation [27–29]. For instance, some catalysts (TiO$_2$, ZnO, CdS, etc.) have been interacted with nanofibrous membranes to achieve photocatalytic removal of organic pollutants [30–33]. As one of the most promising photocatalytic materials, ZnO is typically used to decorate the nanofiber membranes for water purification due to its high photocatalytic activity, low cost, non-toxicity and environmentally friendly feature [34,35]. For instance, Lv et al. fabricated a polyvinyl alcohol and konjac glucomannan based nanofibrous membrane loaded with ZnO nanoparticles via electrospinning and heat cross-linking. The resultant membrane exhibits not only favorable air-filtration performance but also excellent photocatalytic and antibacterial activities [36]. Similarly, Lu et al. reported a multifunctional ZnO/polyaniline/polyacrylonitrile nanofiber membrane by electrospinning and hydrothermal synthesis for oily-wastewater remediation, delivering excellent photocatalytic degradation ability for dyes and antibacterial activity [37]. Moreover, the membrane with micro/nanosized pore structures can also be used to filtrate various oil-in-water emulsions. However, there are several main drawbacks in ZnO based photocatalytic membranes: (i) the adsorption band of ZnO located at the UV region due to its wide band gap value ($E_g= \sim 3.37$ eV), reducing ZnO based nanofiber membrane's service life due to the decomposition of polymeric substrate under UV illumination; (ii) the rapid recombination of photoinduced charge carriers (e$^-$ & h$^+$) in photocatalysis [38,39]; (iii) the dull wettability originated from its hydrophilicity cannot meet different separation occasions. Although several attempts have been adopted to enhance the visible light activity of ZnO, including metal doping, morphology control and heterojunction construction [40–42]. The elaborate and complicated operation and high costs make it difficult to practically scale up; thus, it is critical to investigate a facile and efficient modification method with low cost facilitating the mass manufacturing.

Metal organic frameworks (MOFs), the typical crystalline inorganic-organic hybrid porous materials, which are extensively used in gas separation, gas storage, sensing, photocatalysis and other fields due to their large surface area, high chemical stability, thermal stability and tunable structure [43,44]. Zeolitic imidazolate framework-8 (ZIF-8) composed of Zn^{2+} and 2-methylimidazole (2-Melm) ligands has been employed as functional modifiers in wastewater treatment due to its facile synthesis and stability [45,46]. Recently, some researchers have focused on the fabrication of ZIF-8 based functional membranes. Li et al. demonstrated an inverse deserve beetle-like ZIF-8/polyacrylonitrile composite nanofiber membrane via electrospinning technology for oil-in-water emulsions separation, which shows outstanding emulsions separation and demulsification ability [47]. Ma et al. synthetized a

ZIF-8 @thiolated graphene composites-based polyimide nanofibrous membrane via electrospinning and hydrothermal synthesis [48]. The resultant membrane exhibits high separation efficiency for various oil/water mixtures and water-in-oil emulsions as well as the commendable photocatalytic dye degradation and antibacterial abilities. Similarly, Xie et al. developed a ZIF-8 modified polydopamine coated cellulose membrane by coordination-driven in-situ self-assemble technology, which shows a switchable wettability and high separation efficiency for both oil-in-water emulsions and water-in-oil emulsions [49]. In view of these, there are ample reasons to suggest that ZIF-8 can be used to prepare multifunctional photocatalytic membrane with switchable wettability for water remediation. Unfortunately, ZIF-8 only can be photo-activated by UV illumination due to its wide energy band gap value about 4.9 ~ 5.4 eV, which restricts photocatalytic activity [50, 51].

Structural strength is another crucial factor that affects the durability and stability of nanofiber membranes for long-term filtration. The collected nanofibers on a receiving device are usually arranged randomly and disorderly because the spinning solution jet is in an unstable state during the electrospinning process, resulting in an unsatisfied mechanical property. Although some physical and chemical methods were adopted to create bonding or cross-linking joints between nanofibers, which complicates the preparation and reduces the excellent porosities of original membranes [18]. Therefore, one-step method for reinforcing nanofiber membranes becomes quite attractive. Different substrates including nonwoven fabric, copper mesh and braided tube can be used directly as the supporting substrate to reinforce the mechanical strength [52–54].

Herein, inspired by the multi-scale delicate constructive structure of caterpillar, a worm-like hybrid ZIF-8 @ZnO nanorods anchored on tubular polyvinylidene difluoride (PVDF) nanofibrous membrane (ZZPVDF-TNM) reinforced by a polyester (PET) braided tube is developed. The successful membrane preparation involves multiple techniques including electrospinning and sequent heat-treatment for ZnO seeds conversion, hydrothermal synthesis for ZnO nanowires growth and self-template scarifying method for ZIF-8 generation, which can be served as a superior photocatalytic-separation membrane for organic pollutants degradation and on-demand of emulsions purification. The prepared membranes demonstrate outstanding performance for different pollutants with a high photocatalytic removal efficiency above 99% and commendable emulsion separation efficiency of (up to 99.9% for stable emulsions) under merely gravity-driven mode. Meanwhile, well-aligned ZIF-8 @ZnO nanorods with PET braided tube lining possesses the reinforced strength and enhanced bonding, as well as a switchable surface wettability. Moreover, the organic pollutants adhered to membrane surface can be easily removed under solar light irradiation, resulting in efficient membrane regeneration. Our study provides a new approach for developing of multifunctional membranes to address oil-water emulsion separation and severe fouling concerns for prolonging the worktime of membranes by solar light driven membrane regeneration.

2. Experimental section

2.1. Materials and regents

PVDF powder (Solef 761 A, $Mw \approx 800,000$) was purchased from Solvay, USA. Span 80, n-hexane, dimethylacetamide (DMAc), hexamethylenetetramine (HMTA), zinc acetate dihydrate (Zn(Ac)$_2\cdot$2 H$_2$O), acetone, potassium dichromate (Cr$_2$K$_2$O$_7$), sodium sulphate (Na$_2$SO$_4$), sodium chloride (NaCl), dichloromethane, anhydrous ethanol, silver sulfate (Ag$_2$SO$_4$), sodium dodecyl sulfate (SDS), terephthalic acid (TA) and ammonium hydroxide (NH$_3\cdot$H$_2$O) were provided by Tianjin Kermel Chemical Reagent Co., China. Mercury sulfate (HgSO$_4$), ammonium iron (II) sulfate, rhodamine B (Rh B) and thymol blue (TB) were supplied by Tianjin Wind-ship Chemical Technology Co., China. 2-methylimidazole

(2-Melm), sodium nitrate (NaNO$_3$), sodium carbonate (Na$_2$CO$_3$) and *n*-butanol were acquired from Shanghai Aladdin Bio-Chem Technology Co., China. Kerosene and diesel were acquired from Tianjin Heshilian chemical Co., China. Peanut oil was purchased from local supermarket, Fortune brand, COFCO corporation, China. Bisphenol A (BPA), methylene blue (MB), methyl orange (MO), crystal violet (CV), ethylenediaminetetraacetic acid disodium salt (EDTA-2Na), ferroin, tert-butanol (TBA), benzoquinone (BQ), *L*-histidine (*L*-HIS), 2,2,6,6-tetramethylpiperidin-4-amine (TEMP) and 5,5-dimethyl-1-pyrroline N-oxide (DMPO) were bought from Shanghai Macklin Co., China. The hydrophilic and hydrophobic silica (SiO$_2$) with different particles size (30 nm, 50 nm, 100 nm, 500 nm and 1 μm, respectively) were purchased by Shanghai Pantian Powder Material Co., China. All of above chemical reagents were used directly without any purification.

2.2. Membrane preparation

2.2.1. Fabrication of tubular PVDF nanofiber membranes (PVDF-TNMs)

The required amount of PVDF powders (13 wt%) and Zn(Ac)$_2$·2 H$_2$O (1.5 wt%) were dissolved in a mix solution (acetone to DMAc of 3:7 in mass ratio) and followed by stirring for 24 h at 50 ℃ to get a homogeneous electrospinning doping solution. After that, a commercial electrospinning apparatus (TL-Pro, Tongli, China) was adopted to spin the PVDF doped with Zn(Ac)$_2$·2 H$_2$O onto PET braided tube (PVDF-TNM). Specifically, the electrospinning process was carried out with a high voltage of 15 kV, − 5 kV voltage of collector, a feed rate of 0.6 mL·h^{-1}, and a spinneret to collector distance of 11 cm. Particularly, the PET braided tube (outer diameter ∼ 1.8 mm, Tianjin Boanxin Co., China) was used as a targeted collector with a rotating speed of 1000 rpm. The ambient temperature and relative humidity of spinning environment were controlled at 35 ± 2 ℃ and 65 ± 5%, respectively. After electrospinning, the resulting PVDF-TNMs were placed in a vacuum at 60 ℃ for 24 h to remove the excessive solvent.

2.2.2. Fabrication of ZnO/PVDF-TNMs (ZPVDF-TNMs)

The obtained PVDF-TNMs were subjected to heat treatment at 130 ℃ for 24 h to obtain ZnO seeds, and the heat-treated membranes were denoted as SPVDF-TNMs. Subsequently, the SPVDF-TNMs were placed into a sealed autoclave containing 0.1 M of Zn(Ac)$_2$·H$_2$O and HMTA and maintained at 90 ℃ for 6 h. Finally, the obtained membranes with ZnO nanowires were rinsed with DI water/ethanol for several times, and drying at 70 ℃ to a constant weight and denoted as ZPVDF-TNMs. The detailed reaction mechanism for formation of ZnO seeds and nanowires was displayed in supporting information (section 1.6).

2.2.3. Fabrication of ZIF-8 @ZnO/PVDF TNMs (ZZPVDF-TNMs)

The prepared ZPVDF-TNMs were immersed in a beaker with 13.15 g of 2-Melm and 100 mL 50% ethanol aqueous solution (v/v) for different time intervals (3, 6, 12 and 24 h, respectively) at 20 ℃ so that 2-Melm could adsorb onto the ZnO nanowires and react with Zn^{2+} (by means of self-sacrificing of partial ZnO nanowires) to generate ZIF-8 nanorods layer [20]. After reaction, the resultant membranes were washed with DI water to remove excess reagents and drying to a constant weight at 60 ℃ in vacuum oven. The yielded membranes were defined as ZZPVDF-TNM*x*, where *x* (3, 6, 12 and 24) represents the different immersion time in 2-Melm solution. Accordingly, the membrane samples without PET braided tube (by peeling off the membrane functional layer for testing) were denoted as PVDF (untreated), ZPVDF (heat-treated and ZnO nanowires growth) and ZZPVDF (after ZIF-8 deposition), respectively.

2.3. Characterizations

The surface morphology and elemental composition of membranes was recorded via scanning electron microscope (SEM, Hitachi TM3030, Japan) and field emission scanning electron microscope (FE-SEM,

Hitachi S4800, Japan) equipped with energy dispersive spectrometer (EDS, EDAX Apollo XL, USA). The roughness of membrane surface was detected by a color confocal microscope (CSM, Zeiss 700, Germany). The functional groups and crystalline of prepared membranes were characterized by Fourier transform infrared spectrum (FTIR, Nicolet iS50, USA) under ATR mode and X-ray diffraction (XRD, D8 Discover, Bruker, Germany), respectively. X-ray photoelectron spectrometer (XPS and VB-XPS, Thermo Fisher, USA) was used to detect the surface chemical compositions and valence states of prepared membranes. UV–vis–diffuse reflectance spectra (UV–vis DRS) were measured by an UV–vis NIR spectrometer (UH 4150, HITACHI, Japan) in range from 300 to 1200 nm. The energy band gap value and valance band value (E_{VB}) of prepared membranes were estimated by Eq. (S1) and Eq. (S2) in section 1.1 of supplementary information. The reactive oxygen species (ROS) generated by prepared membranes in photocatalysis were detected via an electron paramagnetic resonance spectrometer (EPR A300, Bruker, Germany) with DMPO as the spin trap agents. Photoluminescence (PL) spectra and time-resolution photoluminescence (TRPL) spectra were measured by a fluorescence spectrometer (FLS 1000, Edingburgh Instruments Ltd., UK). The specific surface area of prepared membranes was detected via a fully automated surface area and porosity analyzer (NOVA 4200e, Quantachrome, USA). Various contact angles (CA) for water (WCA), oil (OCA), underwater oil (UWOCA) and underoil water (UOWCA) of prepared membrane surfaces were detected via a contact angle meter (Kruss, JYSP-180, Germany) with droplet volume around 0.5 μL (DI water-WCA, kerosene-OCA & UOWCA and dichloromethane-UWOCA). Zeta potential of prepared membranes was measured by a solid surface Zeta potential analyzer (Surpass-3, AntonParr, Austria) with pH values of 3 ∼ 10.

Mechanical properties of membranes were measured by electronic tensile testing machines (JingBo Testing Machinery Co., Ltd., Yangzhou, China) in room temperature; the tensile speed rate and gauge were set at 0.5 mm•min^{-1} and 50 mm, respectively. The porosity (ε) of prepared membranes was detected via a dry-wet method using *n*-butanol as the immersion liquid and calculated as following Eq. (1):

$$\varepsilon(\%) = \frac{W_1 - W_0}{\left(\frac{\pi}{4}\right)\left(D^2 - d^2\right)l\rho} \times 100\%\#$$ (1)

where ε is the porosity (%) of membranes; W_1 and W_2 represent the wet mass (immersed in *n*-butanol for 60 min) and dry mass (dried in an oven at 60 ℃ for 12 h) of membranes; ρ is the density of *n*-butanol (0.81 g·cm^{-3}); D, d and l is the outer diameter (cm), inner diameter (cm) and length (cm) of membranes, respectively.

2.4. Analytical methods

2.4.1. On-demand emulsions separation performance

Oil-in-water surfactant-free emulsions (O/WSFEs) and water-in-oil surfactant-free emulsions (W/OSFEs): for O/WSFEs preparation, 1 mL of oil (i.e., *n*-hexane, dichloromethane, kerosene, diesel and peanut oil) was respectively added into 99 mL of DI water. And the mixtures were sonicated for 30 min with 40 kHz and mechanically stirred (1000 rpm) for 12 h to obtain the various milky O/WSFEs. As for W/OSFEs, 1 mL of DI water was added in 99 mL of various oils, followed by sonication and stirring as same as mentioned above.

Oil-in-water surfactant stabilized emulsions (O/WSSEs) and water-in-oil surfactant stabilized emulsions (W/OSSEs): for O/WSSEs, 0.2 mg·mL^{-1} SDS was pre-dissolved in 99 mL of DI water, then 1 mL of oil was added in it. And the mixtures were sonicated for 30 min at 40 kHz and mechanically stirred (1000 rpm) for 12 h to obtain the milky surfactant stabilized emulsions with different oils; as for W/OSSEs preparation, 1 mL of DI water was added in 99 mL of various oils containing 0.1 g Span 80. The mixtures were sonicated and stirred as same as mentioned above. Both of them can retain absolutely stable as least 7 days without any change. The digital photographs of above emulsions

were collected in Fig. S1 and S2.

Emulsion separation: the emulsion separation performance of prepared membranes was investigated by gravity-driven method. Briefly, the membrane was pre-wetted by water or oil and fixed vertically in a glass tube and then various oil-in-water emulsions or water-in-oil emulsions were transferred into the glass tube for separation. Specifically, to obtain a stable flux and accurate separation efficiency, the height of emulsion in glass tube was controlled at $\sim$ 15.0 cm (totally submerged membrane module guaranteed). The permeation flux J (L·m^{-2}·h^{-1}) and separation efficiency (%) can be calculated by Eqs. (2) and (3):

$$J = \frac{V}{A \times T}\#$$ (2)

$$Separation \quad efficiency = \left(1 - \frac{C_p}{C_f}\right) \times 100\%\#$$ (3)

where V (L), A (m^2), and T (h) represent the liquid permeation volume (water or oil), effective membrane area and operation time, respectively. C_p and C_f were the water (or oil) concentrations of the permeation and feeding solutions, respectively.

The trace water content and oil content in emulsions was measured by Karl Fisher moisture titrator (C20, Mettler Toledo, Switzerland) and UV-Vis spectrophotometer (Purkinje TU1819, Purkinje General Instruments Co., Beijing, China). Additionally, the photographs of permeation and feeding solutions were captured by an optical microscope (BX51, Olympus, Japan). The chemical oxygen demand (COD) contents were measured via a typical potassium dichromate method (see the details in section 1.5 of supporting information).

2.4.2. Photocatalytic performance of as-prepared membranes

The typical photocatalytic degradation performance of prepared membranes was respectively evaluated by removal efficiency of various pollutants (BPA, MB and MO) under simulated solar light (Xenon lamp, HF-GHX-XE-300, Shanghai, China) irradiation with a light intensity of 85 mW·cm^{-2} ($\lambda = 320 \sim 2500$ nm). Briefly, the membrane module (effective membrane area: 6.8 $\sim$ 7.0 cm^2) was placed into a quartz tube containing 20 mL of pollutant solution (10 ppm) with a stirring at the bottom in darkness for 1 h to finish adsorption-desorption equilibrium between pollutants and the membranes. Then, the reaction solution was exposed to solar light illumination and analyzed by an UV-Vis spectrophotometer at different irradiation time intervals (0, 30, 60, 90, 120 min, respectively). Additionally, the photocatalytic removal efficiency can be calculated as Eq. (4):

$$Removal \; efficiency = \left(\frac{C_0 - C_i}{C_0}\right) \times 100\%\#$$ (4)

here, C_0 and C_i were the absorbance of initial pollutant solution and the aliquot after different reaction time. And the distinguished adsorption wavelength of BPA, MB and MO for the assessment of degradation capacity is located at 280 nm, 664 nm and 463 nm, respectively.

To identify the effect of some common inorganic anions in actual wastewater, the membrane was placed in 20 mL of BPA solution (10 ppm) containing 10 mM of different inorganic salts (Na$_2$CO$_3$, Na$_2$SO$_4$, NaNO$_3$ or NaCl, respectively) to carry out the photocatalytic reaction. In order to investigate the effect of real water matrix, 0.0570 g of BPA was dissolved in 20 mL of different real water matrices: tap water (Tianjin, China), seawater (Bohai Bay, Tianjin, China), lake water (Panhu Lake in our campus, Tiangong University, Tianjin, China) and textile wastewater (ZhengDingGuangHua factory, Shijiazhuang, Hebei province, China) to perform the photocatalytic degradation, respectively. And the specific operation and analytic method were similar to ordinary BPA removal test as mentioned above. Here, the turbidity of various real water matrices was detected by a turbidimeter (WZB-175, INESA Scientific Instrument Co., Shanghai, China). In addition, for

natural sunlight photocatalytic reaction, one piece of ZZPVDF-TNM was immersed in 10 mL of various dyeing solution (5 ppm of MB, MO, TB, CV and Rh B, respectively) and irradiated with sunlight in our campus (Tiangong University, Tianjin, China; latitude 39° 3′ 54″ N and longitude 117° 6′ 40″ E); the irradiation time was set as 14:00–17:00 in the afternoon of September (26.5 ℃ $\pm$ 5 ℃), and the maximum and minimum light intensity was 94.35 and 46.48 mW·cm^{-2}, respectively. The leachability of Zn ions in prepared membranes was detected by the Varian Vista MPX inductively coupled plasma optical emission spectrometer (ICP-OES, CCD, USA). The intermediate products of BPA in photocatalytic degradation were determined by a gas chromatography-mass spectrometry system (HPGC-MS, SCION 456-TQ, Scion Instruments Ltd, Germany). The details of theoretical calculation methods and toxicity analysis can be found in section 1.3 of supporting information. The quenching experiments were performed by adding 2 mmol different scavengers (EDTA-2Na for h$^+$, L-HIS for ^{1}O$_2$, BQ for·O$_2^-$ and TBA for·OH, respectively) into 20 mL of BPA solution (10 ppm) with a piece of as-prepared ZZPVDF-TNM to investigate the contribution of ROS and h$^+$.

2.4.3. Anti-fouling performance and membrane regeneration

Anti-fouling performance of prepared membranes was conducted by a four-step of continuous filtration process in gravity mode as follows: the water flux of prepared membrane based on pure water permeation was denoted as J_W; subsequently, the surfactant stabilized kerosene-in-water emulsion was filtrated by the membrane, and the filtration flux was denoted as J_E; then, the contaminated membrane was rinsed with DI water for 30 min, and then the recovered water flux was denoted as J_{R-W} [15]. Specifically, the rinsed membrane was irradiated with a 300 W Xenon lamp for 60 min and the recovered flux was named as J_{R-I}. The calculation method of various anti-fouling indices was listed in section 1.7 of supplementary information.

As for membrane regeneration, the fouled membranes (after 5 times use of emulsion filtration or photodegradation of pollutants) were placed in a quartz beaker containing DI water and illuminated by a Xeon lamp for 60 min under constantly and gently magnetic stirring at the bottom to remove the contaminants for the next cycle of use.

### 2.4.4. Simultaneous removal performance to complex oily-wastewater

The complex oily-emulsion filtration with dye and/or surfactants were conducted as similar as ordinary emulsion separation in gravity-driven mode. Briefly, a defined amount of target pollutants (5 ppm of MB or BPA) was dissolved in surfactant free and surfactant stabilized kerosene-in-water emulsions, respectively. And then, the separation operation was performed under light irradiation or without light, respectively. The seed breeding experiments were performed for reflecting the simultaneous removal performance to complex oily-wastewater based on statistical germination rate, and the details are described in experimental section 1.4 of supporting information. In addition, the details of SiO$_2$ suspensions filtration test were described in section 1.2 supporting information.

3. Results and Discussion

3.1. Morphology and chemical structure of multifunctional ZIF-8 @ZnO PVDF catalytic tubular nanofiber membrane

Constructing a well-aligned ZIF-8 @ZnO nanorod arrays on membrane surface is crucial for improving the photodegradation and demulsification performance of membranes. As depicted in Fig. 1a & b, the fabrication strategy of ZZPVDF-TNM included four steps: electrospinning, heat-treatment, hydrothermal and chemical self-template scarified reactions. During the initial fabrication process, an electrospun nanofiber membrane with multi-interconnected channel structure reinforced by PET braided tube was obtained by PET tube as a receiver. It can be observed that the PVDF nanofiber membrane adheres tightly to
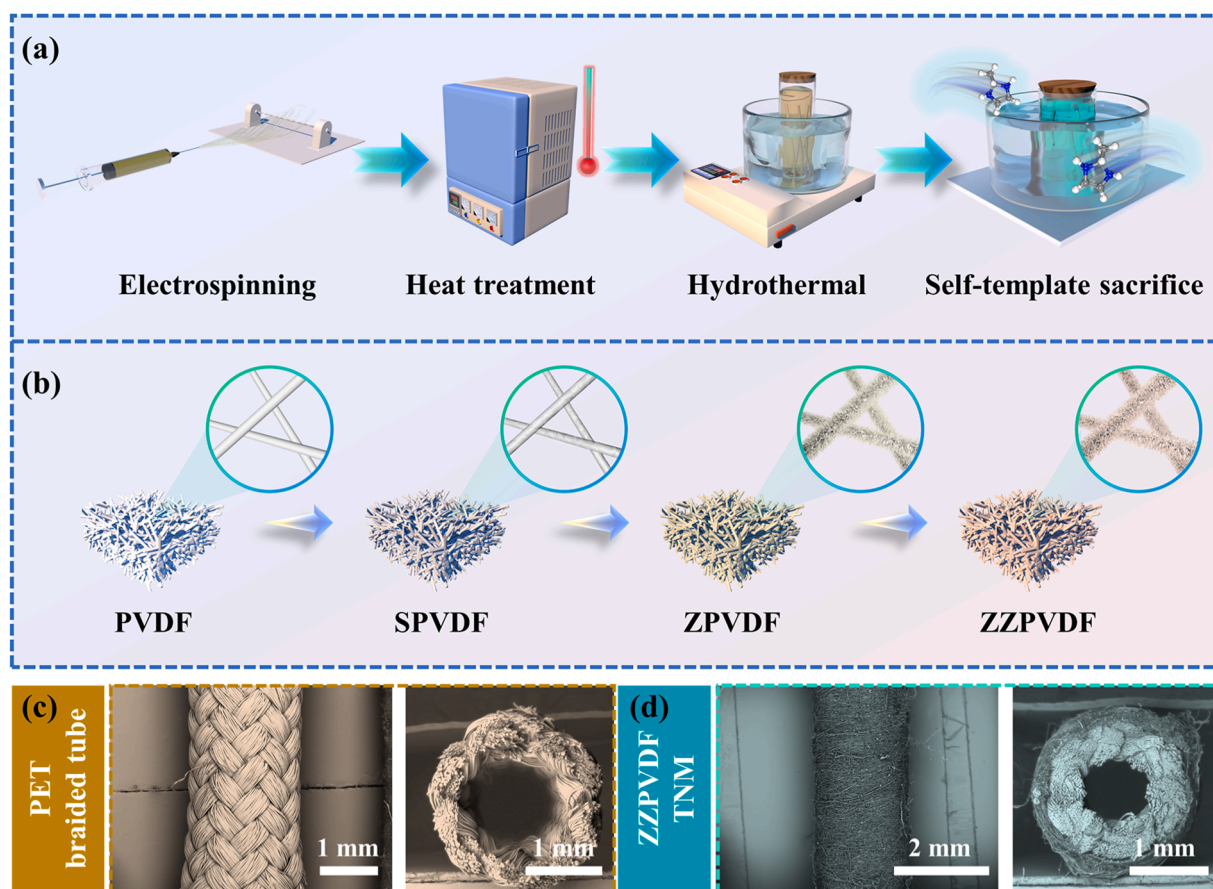
Fig. 1. (a) Schematic illustration of the preparation process of ZZPVDF-TNM; (b) the sequential evolution illustration of as-prepared nanofiber membrane layer; SEM images and cross-sectional view of (c) PET braided tube and (d) ZZPVDF-TNM.

PET braided tube which enhances the self-supporting and mechanical properties (Fig. 1c & d). Obviously, as-spun PVDF nanofibrous membrane possess the porous structure formed by the randomly intersecting stacked nanofibers with relatively smooth surface (Fig. 2a & b). After heat-treatment, the surface of nanofiber membrane become coarser than that of pristine PVDF nanofiber membranes; and numerous granules appear on nanofibers, which can be attributed to ZnO seeds from Zn (Ac)$_2$·2 H$_2$O thermal conversion by dehydration and decomposion (Fig. 2c & d & i) [55]. These ZnO seeds provide a favorable foundation for the growth of ZnO nanowires, that is, the fully-exposed and anchored ZnO crystal seeds roughen the nanofiber surface, which facilitates the induced crystallization and in-situ growth of ZnO nanowires. Fig. 2e & f clearly demonstrate that needle-like ZnO nanowires uniformly appear on the PVDF nanofiber membrane after hydrothermal reaction. The adequate ZnO nanowires provides the initial wettability for membranes and the intended sacrificial template for the subsequent ZIF-8 growth. As shown in Fig. 2g & h, the ZnO becomes shorter and rougher, and the nanorods are formed with the rods' length and width of ∼ 1.45 μm and 0.15 μm, respectively, which demonstrates the ZIF-8 nanocrystals have been decorated on the membrane surface after reacting with 2-Melm. Furthermore, the influence of reaction time (immersion time) was investigated. As the membrane is directly immersed in a low constant temperature 2-Melm solution without any operation, a relative long immersion time is necessary for the conversion of ZnO to ZIF-8. When the immersion time is insufficient, only a little amount of ZnO nanowires can be transformed into ZIF-8; while too much time is spent, the ZnO nanowires will be completely etched, and ZIF-8 nanoparticles aggregate and accumulate on the fiber surface densely, resulting in the blockage of the pores and channels [20]. The optimum immersion time is 12 h in the 2-Melm solution for ZIF-8 growth (Fig. S3).

Meanwhile, the signals of Zn, C, O and N can be detected uniformly on nanofiber membrane, as shown in EDS results of Fig. S4, which further confirmed that ZnO@ZIF-8 nanorods have been homogenously anchored on the tubular PVDF nanofibrous membranes. The 3D LCSM results reveals that the surface roughness value (R_a) of ZZPVDF membrane is significantly higher than that of pristine PVDF membrane (Fig. 2i). And the maximum R_a value of 2.38 μm can be achieved by the decoration of ZnO@ZIF-8 nanorods, which endows the ZZPVDF-TNM with a robust superamphiphilic/under-liquid superamphiphobic ability according to Cassie's law. Additionally, R_a values of ZZPVDF membrane with different immersion time in 2-Melm solution also indicate that a suitable reaction time will facilitate the transformation from ZnO to ZIF-8 and the enhancement of the surface roughness, leading to the improvement of the photocatalytic and oil-water separation performance (Fig. 2j & Fig. S3d). As depicted in Fig. 2k, the resultant membrane shows a superamphiphilicity in air; water or oil droplets spread rapidly on the membrane surface. After prewetted by oil or water, the membrane surface can repel the water or oil droplet, showing a potential under-liquid dual superamphiphobicity. By virtue of the simply controllable method, ZZPVDF-TNM can be facilely fabricated in quantities as depicted in Fig. 2l.

The phase structure and chemical compositions of prepared membranes were further investigated by XRD and FTIR. As shown in Fig. 3a, the specific adsorption peaks at 840, 879, 1072, 1169 and 1278 cm^{-1} are corresponded to the typical β-phase of PVDF [56,57]. The electric dipoles arranged randomly in PVDF doping solution can be realigned and reoriented under a high voltage during electrospinning process. And these peaks also can be observed in ZPVDF and ZZPVDF. Moreover, the intensity of typical β-phase adsorption peaks is enhanced in ZPVDF and ZZPVDF, demonstrating the β-phase crystallization is promoted after
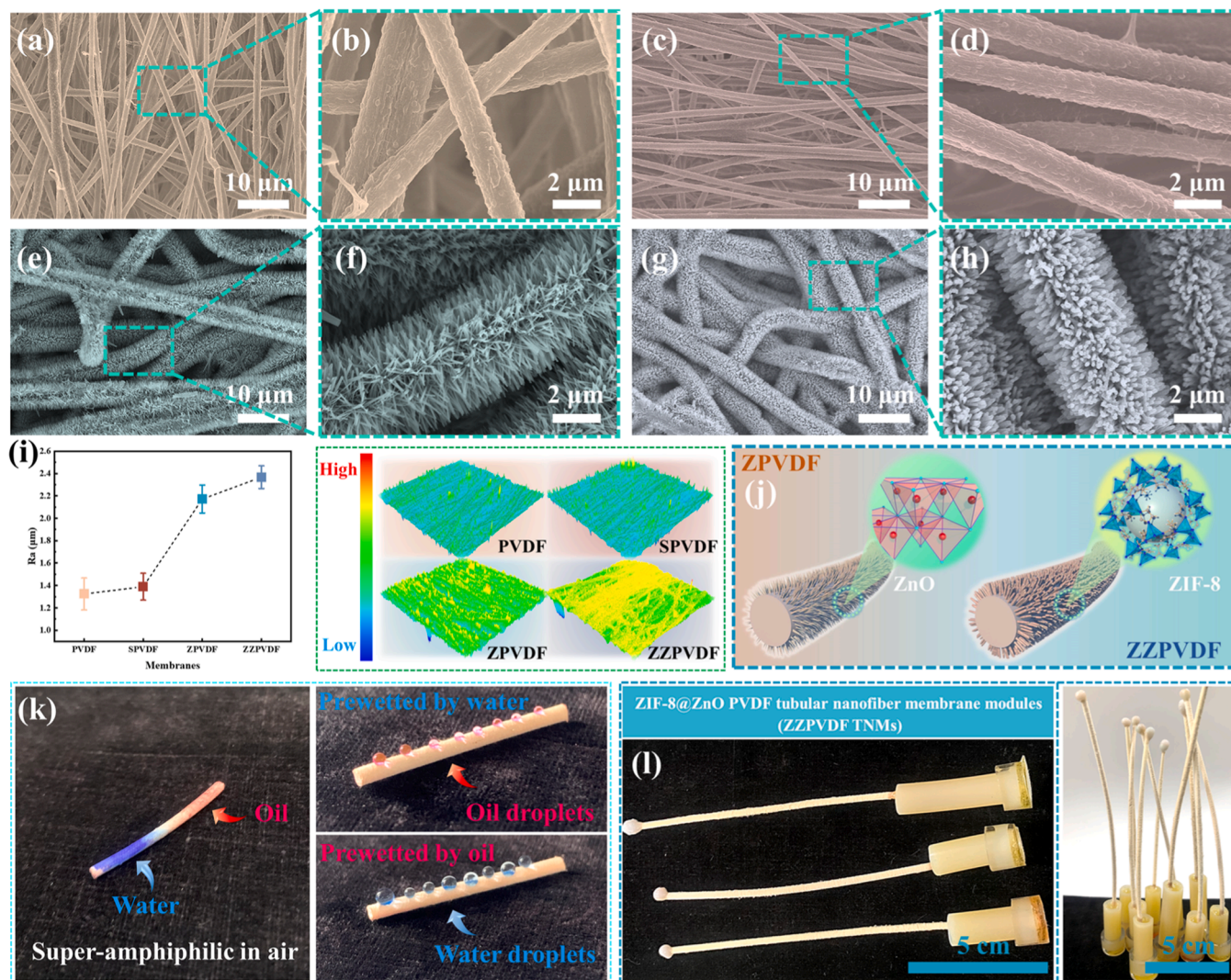
Fig. 2. SEM images of (a) & (b) PVDF, (c) & (d) SPVDF, (e) & (f) ZPVDF and (g) & (h) ZZPVDF; (i) 3D optical profilometry images and corresponding R_a values of as-prepared membranes; (j) schematic diagram of ZPVDF and ZZPVDF; optical photos of special wettability of (k) ZZPVDF-TNM and (l) membrane modules.

hydrothermal process. The adsorption peaks at 2929 cm^{-1} and 3134 cm^{-1} can be ascribed to the imidazole ring and C-H bonds of methyl in ZIF-8, respectively [58,59]. As shown in Fig. 3b, the typical diffraction peak at $2\theta = 20.5°$ can be clearly observed, which is ascribed to the β-phase of PVDF molecular chains, demonstrating the transformation of polar β-phase crystalline from α-phase crystalline of PVDF powders as reported in literature [60]. After hydrothermal reaction, some diffraction peaks appeared at 2θ of 31.8°, 34.5°, 36.4°, 47.6°, 56.7°, 62.9° and 69.1° are attributed to the (100), (002), (101), (102), (110), (103) and (112) crystal planes of hexagonal wurtzite structure of ZnO (JCPDS No. 36–1451), indicating that the hexagonal ZnO nanowires formed uniformly and steadily on the membrane surface [55,57]. Obviously, the diffraction peaks of ZPVDF are narrow and sharp, demonstrating the highly crystalline nature of ZnO nanowires. For ZZPVDF, the new peaks at 2θ of 7.4°, 10.5°, 12.6°, 14.6°, 16.8°, 18.2°, 24.6° and 26.8° are corresponded to (011), (002), (112), (022), (013), (222), (224) and (134) crystal planes of ZIF-8 with zeolite structure, which is consistent with simulated single crystalline phase of ZIF-8 [61]. Meanwhile, the diffraction peaks of hexagonal ZnO are maintained without disruption, suggesting that the partial ZnO nanowires on membrane has been transformed into ZIF-8; these nanorods together with intact ZnO form a ZnO@ZIF-8 heterojunction.

The chemical states and elemental compositions of prepared

membranes are detected by a high-resolution XPS (Fig. 3c). The intense signals of C 1 s and F 1 s can be clearly observed; and the faint signals of O 1 s and Zn 2p also can be detected in pristine PVDF membrane. After heat-treatment and hydrothermal process, the signal intensity of Zn 2p and O 1 s is prominent, indicating ZnO has been successfully anchored on PVDF membrane surface (Fig. 3d). As shown in Fig. 3e, a conspicuous new signal is attributed to N 1 s in ZZPVDF membrane, which reveals that a partial of ZnO nanowires have transformed into ZIF-8, forming a ZnO@ZIF-8 heterojunction structure. By the fitting of the N 1 s spectrum using 2 peaks situated at 398.12 and 389.73 eV, the pattern can be corresponded to N atom of imidazole linkers and Zn-N bonds, respectively (Fig. 3e) [62]. As displayed in Fig. 3f, O 1 s curve can be deconvoluted into two peaks located at 530.78 and 531.76 eV in ZPVDF, which are credited to O^{2-} ions and oxygen vacancy of hexagonal ZnO in membranes, respectively. In general, more oxygen vacancy sites will facilitate the photocatalytic reaction due to its high atmospheric O$_2$ adsorption capacity [63]. A small negative shift of O 1 s peak in ZZPVDF can be associated to the interfacial charge transfer from ZIF-8 to ZnO. Fig. 3g displays the Zn 2p spectra, in which Zn 2p $_{3/2}$ and Zn 2p $_{1/2}$ orbitals are respectively located at 1021.81 eV and 1044.81 eV, which matches the binding energy of Zn^{2+} in ZnO. Specifically, the peaks of Zn^{2+} in ZZPVDF located at 1021.51 eV and 1044.51 eV are slightly blue shifted than the binding energy of ZPVDF, which can be ascribed to the
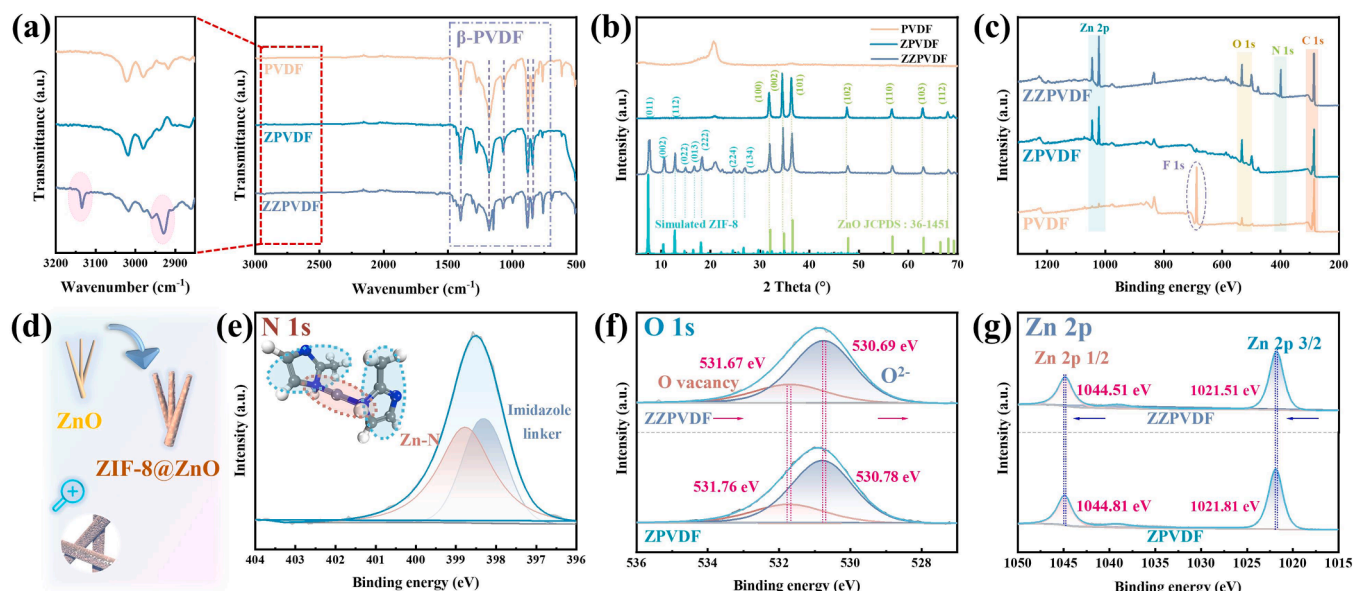
Fig. 3. (a) FTIR spectra, (b) XRD patterns and (c) XPS survey scanning spectra of as-prepared membranes; (d) schematic illustration of ZnO nanowires and ZIF-8 @ZnO nanorods; (e-g) high resolution spectra for N 1 s, O 1 s and Zn 2p.

enhancement of electron density for Zn 2p orbitals in ZnO@ZIF-8 heterostructure [51,64]. Thus, all of above results prove that ZIF-8 @ZnO heterojunction structure has been successfully synthetized on the PVDF-TNM surface.

3.2. Permeability and mechanical properties of as-prepared membranes

Generally, the permeation ability of membrane depends on its pore structure. As shown in Fig. 4a, during the electrospinning process, the nanofibers will be stacked layer by layer to form a loose and porous network structure, resulting in a porosity of as high as 68.59% of pristine PVDF-TNM. The porosity maintains at 70. 32% with no significant change after heat treatment, indicating that the loose and porous skeletal structure was not destroyed. After hydrothermal reaction, ZnO nanowires are uniformly distributed on the nanofiber membrane with a compact structure. The nanofiber skeleton is almost totally covered by ZnO nanowires, leading to the blocked pores filled with ZnO and a remarkable decreased porosity of 56.97%. Although the ZnO nanowires reduce, to some extent, the porosity of ZPVDF-TNM, which can form interconnected subchannels, promoting the sieving function of membranes. As the ZnO nanowires as a template directly react with 2-Melm, the intense nanowires can be converted into rough nanorods in this process, leading to a slight increased porosity (60.34%) of ZZPVDF-TNM than before conversion. As depicted in Fig. 4b, the well-grown ZnO@-ZIF-8 nanorods along with the tightly wrapped PVDF nanofibrous skeleton structure on PET braided tube decreases the average pore size

of membranes from 2.01 μm to 0.55 μm. The results suggests that the sieving effect of the ZZPVDF-TNM will be enhanced, which improves the complex wastewater separation capability. On the one hand, the narrow pore width could enhance the filtration performance of various emulsions. On the other hand, it also acts as a micro catalytic reactor providing the constrained space to closely contact with the organic pollutants for photocatalytic degradation. Water and kerosene are respectively employed to investigate the permeation performance of prepared membranes. As shown in Fig. 4c, due to the robust hydrophobicity of PVDF molecules, it is difficult for pure water to completely wet the PVDF nanofiber by gravity-driven action only, hence the pure water flux of PVDF-TNM and SPVDF-TNM is extremely low (148 and 235 $L \cdot m^{-2} \cdot h^{-1}$, respectively). For ZPVDF-TNM, with the help of a large number of hydrophilic ZnO nanowires immobilized on nanofiber surface, the membrane surface can be rapidly wetted by pure water [55]. This accounts for the enhanced water flux up to 880 $L \cdot m^{-2} \cdot h^{-1}$. Also, ZZPVDF-TNM exhibits hydrophilic properties and commendable water flux of 784 $L \cdot m^{-2} \cdot h^{-1}$, despite a decrease due to the smaller pore size than that of ZPVDF-TNM. On the other hand, the oil fluxes of PVDF-TNM (1320 $L \cdot m^{-2} \cdot h^{-1}$) and SPVDF-TNM (1500 $L \cdot m^{-2} \cdot h^{-1}$) are significantly higher than ZPVDF-TNM (67.5 $L \cdot m^{-2} \cdot h^{-1}$) due to its undesirable wettability by kerosene phase with OCA of 81.5°. Interestingly, thanks to the amphiphilic nature of ZZPVDF-TNM after ZIF-8 formation, it can also be wetted by oil with a high oil flux of 864.5 $L \cdot m^{-2} \cdot h^{-1}$.

As shown in Fig. 5a, the thickness of pristine PVDF-TNM decreases from 1.73 mm to 1.61 mm after half an hour of heavy pressure with
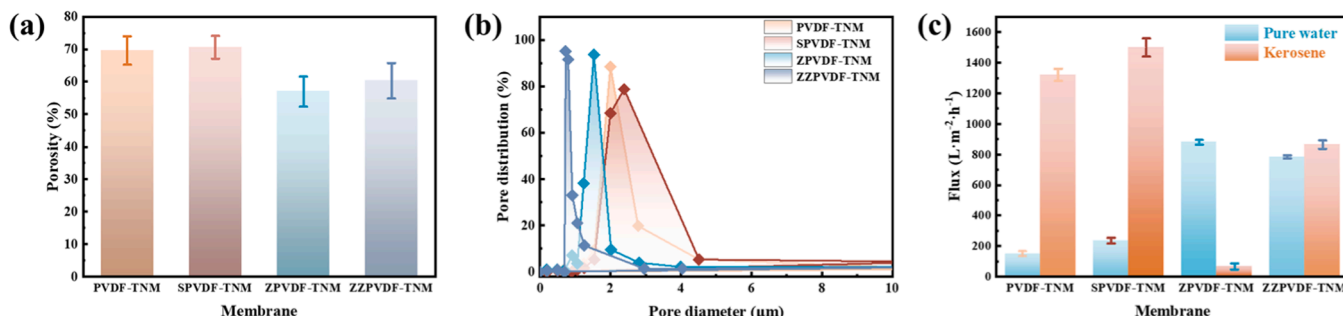
Fig. 4. (a) Porosity, (b) pore size distribution, (c) water and kerosene flux of as-prepared membranes.
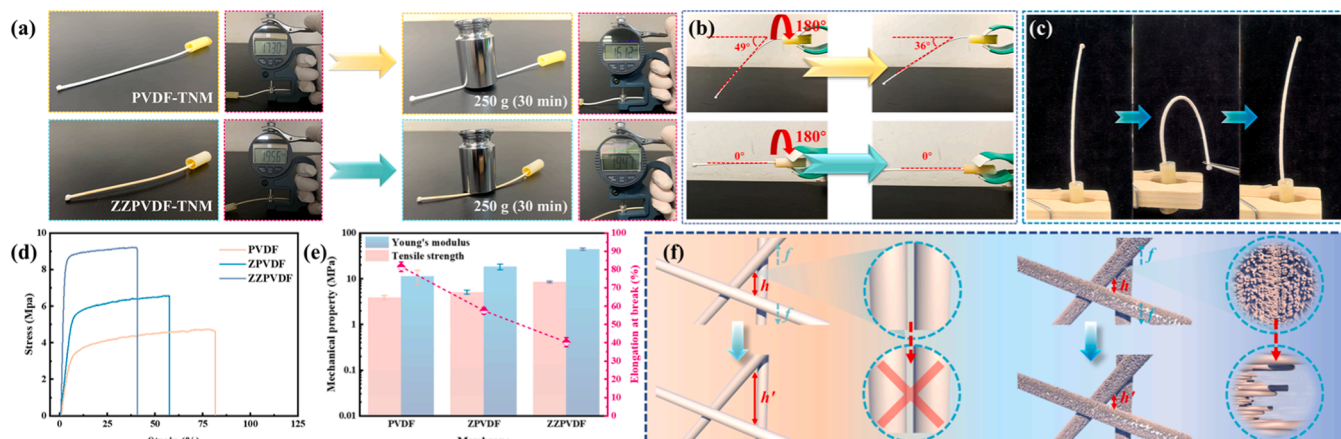
Fig. 5. (a) PVDF-TNM and ZZPVDF-TNM with loaded weight of 250 g for 30 min; (b) self-supporting property and (c) bendability of ZZPVDF-TNM; (d) stress-strain curves and (e) anti-comprehensive properties of as-prepared membranes; (f) schematic illustration of entangled and interlocked nanofibers in as-prepared PVDF-TNM and ZZPVDF-TNM.

250 g weight, with a 6.82% reduction, but still maintains its hollow tube shape, indicating that the PET braided tube significantly reinforced the anti-compressive and self-supporting properties of the tubular nanofiber membranes. More importantly, the resultant ZZPVDF-TNM exhibits an excellent self-supporting performance with almost no change in thickness after removal of heavy pressure with the same weights, showing a good resiliency of up to 99.54% (Fig. 5a). As can be seen from Fig. 5b, after self-rotation along with the axis direction, pristine PVDF-TNM membrane has a significant bending effect with a downward angle of 36° than that before rotation of 49° under gravity. In comparison, ZZPVDF-TNM presents a commendable stiffness with a horizontal angle of ~0°, showing the excellent self-supporting property. Moreover, when the membrane module was bent (fold the membrane with a rotation angle of 180°), after external force released, the membrane module will recover its initial situation (Fig. 5c), which demonstrates that the

ZZPVDF-TNM possesses a superior shape recovery.

The mechanical properties of the membrane layer (peeled off from PET braided tube) are further analyzed as illustrated in Fig. 5d & e. The pristine PVDF nanofiber membrane is easily deformed under a minor force with a low tensile strength (4.22 MPa) and low Young's modulus (11.26 MPa). The mechanical strength of ZPVDF goes up to 6.17 MPa for tensile strength and 18.05 MPa for Young's modulus, which can be probably attributed to the enhanced interaction and friction effect (Fig. 5f) between the ZnO nanowires, resulting in the formation of interlocking structures and the reduction of slip-deformation in PVDF nanofibers. The originally smooth ZnO nanowires gradually become rougher after the decoration of ZIF-8, and the interactions between nanofibers in ZZPVDF will be further enhanced, inducing a further increase of 9.39 MPa for tensile strength and 43.98 MPa for Young's modulus. However, the stretching effect between the nanofibers is
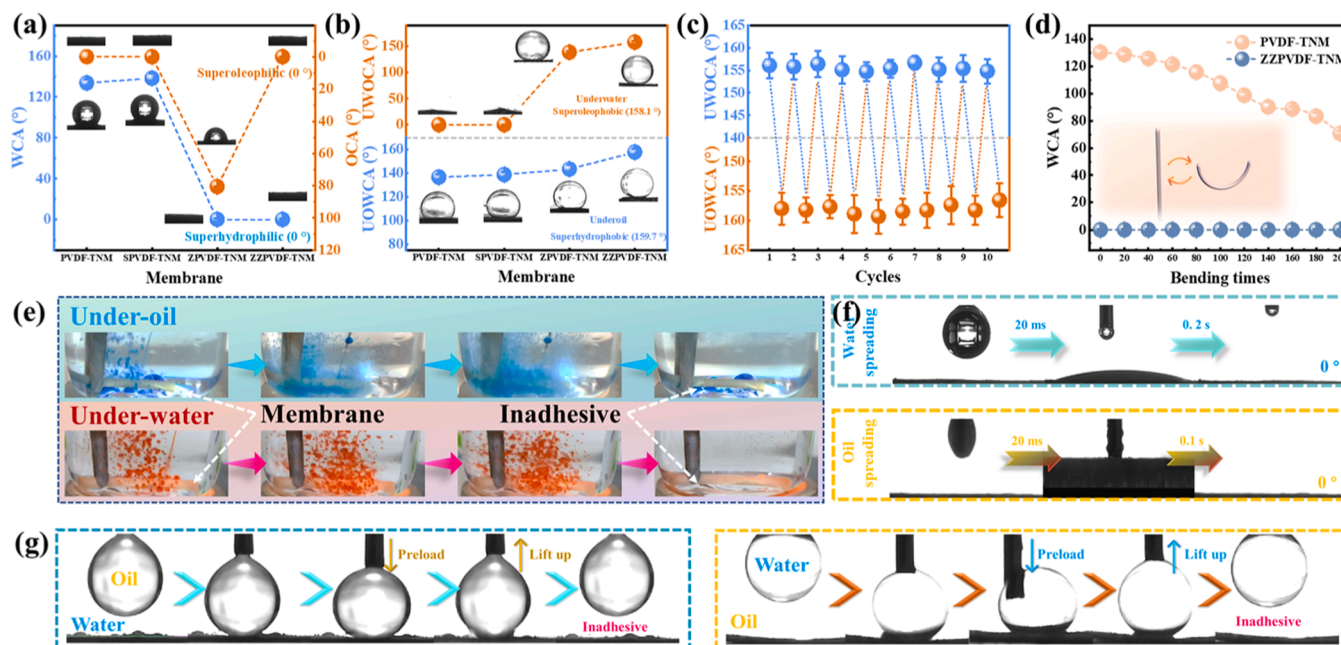
Fig. 6. (a) WCA and OCA of as-prepared membranes; (b) UWOCA and UOWCA of as-prepared membranes; (c) reversible wettability switch between underwater superoleophobicity and underoil superhydrophobicity for 10 cycles; (d) WCA of PVDF-TNM and ZZPVDF-TNM within 200 bending times; (e) optical images of underoil anti-water-adhesion (water dyed by MB) performances and underwater anti-oil-adhesion (oil dyed by Sudan III) of ZZPVDF-TNM; (f) water and oil spreading process in air on ZZPVDF-TNM surface; (g) photographical evolution of underwater dynamic oil repelling (left inset) and underoil water repelling behaviors (right inset) of ZZPVDF-TNM.

weakened after the decoration of ZnO nanowires or ZnO@ZIF-8 nanorods, showing a decreased elongation at break. The breaking strength show an order of ZZPVDF nanofiber membrane > ZPVDF nanofiber membrane > pristine PVDF nanofiber membrane; and the breaking elongation of prepared nanofiber membranes is in the order of PVDF (81.59%) > ZPVDF (57.51%) > ZZPVDF (40.3%).

3.3. Reversible super wettability of membranes

The surface wettability of prepared membranes is determined by water and oil contact angles (WCA & OCA) in air and under liquid conditions. As depicted in Fig. 6a, the pristine PVDF-TNM displays hydrophobic property with a WCA of 133.6° due to its low surface energy and rich C-F bonds. After heat-treatment, the SPVDF-TNM shows a slightly increased WCA (138.27°) than that of PVDF-TNM. However, ZPVDF-TNM and ZZPVDF-TNM demonstrate a super-hydrophilicity with WCA of 0° in air. After the growth of ZnO nanowires on PVDF nanofibers, the hydrophilicity of membrane is significantly enhanced, which is mainly attributed to the unique multi-substructure and intrinsic hydrophilicity of ZnO nanowires. Based on the Wenzel theory, the higher roughness of the hydrophilic surface is, the better hydrophilicity reaches, so the ZZPVDF-TNM surface exhibits super hydrophilicity in air [25,52]. It is clearly that prepared membranes exhibit an oleophilic property with OCA of 0° other than ZPVDF-TNM with OCA of 81.5°. Overall, prepared ZZPVDF-TNM display a satisfactory super-amphiphilicity in air. As shown in Fig. 6f, both the water and oil droplet can rapidly spread out and permeate into the ZZPVDF-TNM within 0.2 s, indicating the excellent superamphiphilicity.

As shown in Fig. 6b, the UWOCA of PVDF, SPVDF, ZPVDF and ZZPVDF-TNM is 0°, 1.6°, 138.7° and 158.1°, respectively, indicating that ZZPVDF-TNM exhibits an underwater superoleophobicity. And the UOWCAs of these membranes are 136.7°, 138.8°, 143.6° and 159.1°, respectively, suggesting that ZZPVDF-TNM also exhibits an excellent underoil superhydrophobicity. The above results demonstrate that the resultant ZZPVDF-TNM shows under-liquid superamphiphobicity (both UWOCA and UOWCA >150°), which indicates that the membrane is probably employed to separate both oil-in-water and water-in-oil emulsions [19]. Moreover, a reversible wettability transition can be achieved by simple washing with water and ethanol (Fig. 6c), the UWOCA and UOWCA of ZZPVDF-TNM remain really stable (>150°) after multiple transitions, which further verifies the potential of ZZPVDF-TNM for the separation of different types of oil-water emulsions. After 200 bending cycles (on consideration of extreme case), as depicted in Fig. 6d, the WCA of pristine PVDF-TNM decreases from 133.6° to 73.4°, which is mainly attributed to the disruption of PVDF nanofiber layer on the PET braided tube; whereas the WCA of ZZPVDF-TNM remains its super hydrophilicity without any deterioration.

The liquid jet (water dyed by MB and oil dyed by Sudan III, respectively) can be immediately bounced off ZZPVDF-TNM's surface without any stickiness, suggesting that the prewetted liquid (oil or water) acts as a liquid barrier layer to avoid the permeation of water or oil (Fig. 6e). In practical oil/water filtration process, the membrane surface mainly interacts with the second-phase liquid (water or oil), thus the under-liquid dynamic wetting behavior of the ZZPVDF-TNM can reflect the underwater oil repelling and underoil water repelling capacity. As illustrated in Fig. 6g, an oil droplet or water droplet is pre-loaded to approach and squeeze toward the ZZPVDF-TNM under liquid, and then it can be lifted from membrane surface. In this process, the oil droplet (water droplet) retains a nearly spherical shape underliquid, indicating the superior low oil adhesion (low water adhesion) and underwater oil-repelling properties (underoil water-repelling properties) [65]. The micro-nano multilevel architecture and suitable surface constructed by ZIF-8 @ZnO nanorods can repel water or oil droplets based on a stable liquid barrier interface, showing a superior under-liquid superamphiphobicity. Fundamentally, the wettability and solid-liquid

adhesion properties of membranes are dominated by nanoarchitecture of membrane surface. The adhesion properties are strongly dependent on the micro/nano structure of the membrane surface. Benefiting from the dense and rough ZIF-8 @ZnO nanorods layer, the water phase or oil phase can be firmly bound around the nanorods to construct a close liquid layer [66]. When the membrane is subjected to the oil pressure (water pressure) underwater (underoil), the water molecules (oil molecules) in the relentless liquid layer can act as a barrier layer to avoid the penetration of oil phase (water phase), showing the underwater oil repelling or underoil water repelling properties of ZZPVDF-TNM.

3.4. On-demand of emulsions stable separation

Oil/water separation performance is vital for oily-wastewater treatment, here, the surfactants free and surfactants stabilized kerosene/water emulsions (kerosene-in-water and water-in-kerosene emulsions) are used to evaluate the emulsion separation performance of prepared membranes. As shown in Fig. 7a & d, for surfactants free kerosene/water emulsion, PVDF-TNM and SPVDF-TNM present a lower water flux to kerosene-in-water emulsion of 22.4 L·m^{-2}·h^{-1} & 39 L·m^{-2}·h^{-1} and higher oil flux to water-in-kerosene emulsion of 118.3 L·m^{-2}·h^{-1} & 126.5 L·m^{-2}·h^{-1}, respectively. The lower separation efficiency of about ~ 60% demonstrates that the pristine membrane and heat-treatment membrane fail to perform emulsion separation effectively. The appreciable separation efficiency (~ 93%) of ZPVDF-TNM is much higher than that of PVDF and SPVDF-TNM for both O/WSFE and W/OSFE, however, the low filtration flux of merely 44.38 L·m^{-2}·h^{-1} for water-in-kerosene emulsions is unsatisfied due to the strong oleophobicity of ZnO nanowires. After decorated by ZIF-8, the wettability and underliquid amphiphobicity of ZZPVDF-TNM are considerably enhanced, resulting in excellent emulsion separation efficiency (99.85% and 99. 92% for kerosene-in-water and water-in-kerosene emulsions, respectively) with high filtration flux (76.4 L·m^{-2}·h^{-1} and 90.7 L·m^{-2}·h^{-1} for kerosene-in-water and water-in-kerosene emulsions, respectively). As shown in Fig. 7b, there are some differences in filtration flux of ZZPVDF-TNM for various W/OSFE (water-in-hexane, water-in-dichloromethane, water-in-diesel and water-in-peanut oil), which may be associated to various oil viscosities. More importantly, emulsion separation efficiency of ZZPVDF-TNM for these emulsions exceed over 99%. In terms of several O/WSFE (hexane-in-water, dichloromethane-in-water, diesel-in-water and peanut oil-in-water), a small drop in the separation efficiency occurs, it still maintains at a high level (> 99% from Fig. 7c). Furthermore, the COD values of various emulsion filtrates are lower than 120 mg•L^{-1} (the limit value of China's wastewater discharge tertiary standard), indicating that the ZZPVDF-TNM can be used to separate the qualitied water from various O/WSFE.

Since the real oily wastewater is always stable in aqueous environment with emulsifiers or surfactants, hence a series of surfactants stabilized emulsions (O/WSSE and W/OSSE) are also employed to evaluate the stable emulsions separation capacity of prepared ZZPVDF-TNM. As shown in Fig. 7d-f, the overall trend of flux and separation efficiency of prepared membranes follow the similar pattern to that of surfactants free emulsions. The separation efficiency of ZZPVDF-TNM for both W/OSSE and O/WSSE is also higher than 97.7%. And the COD values of various emulsion filtrates also remain a low level of < 120 mg•L^{-1}, which further proves that prepared membranes exhibit a favorable separation ability and promise applicability for surfactants stabilized emulsions. As shown in Fig. 7g & h, all of original emulsions is cloudy and non-transparent with a lot of tiny droplets; while the filtrates exhibit a transparent appearance and contain no obvious droplets in the sight of optical microscope, indicating that oil droplets or water droplets can be blocked and separated by ZZPVDF-TNM. The above results have proved that prepared ZZPVDF-TNM has great potential for the high-efficient treatment of a wide range of unstable and stable water-in-oil emulsions or oil-in-water emulsions.

Furthermore, Young's equation and the total interfacial energies of
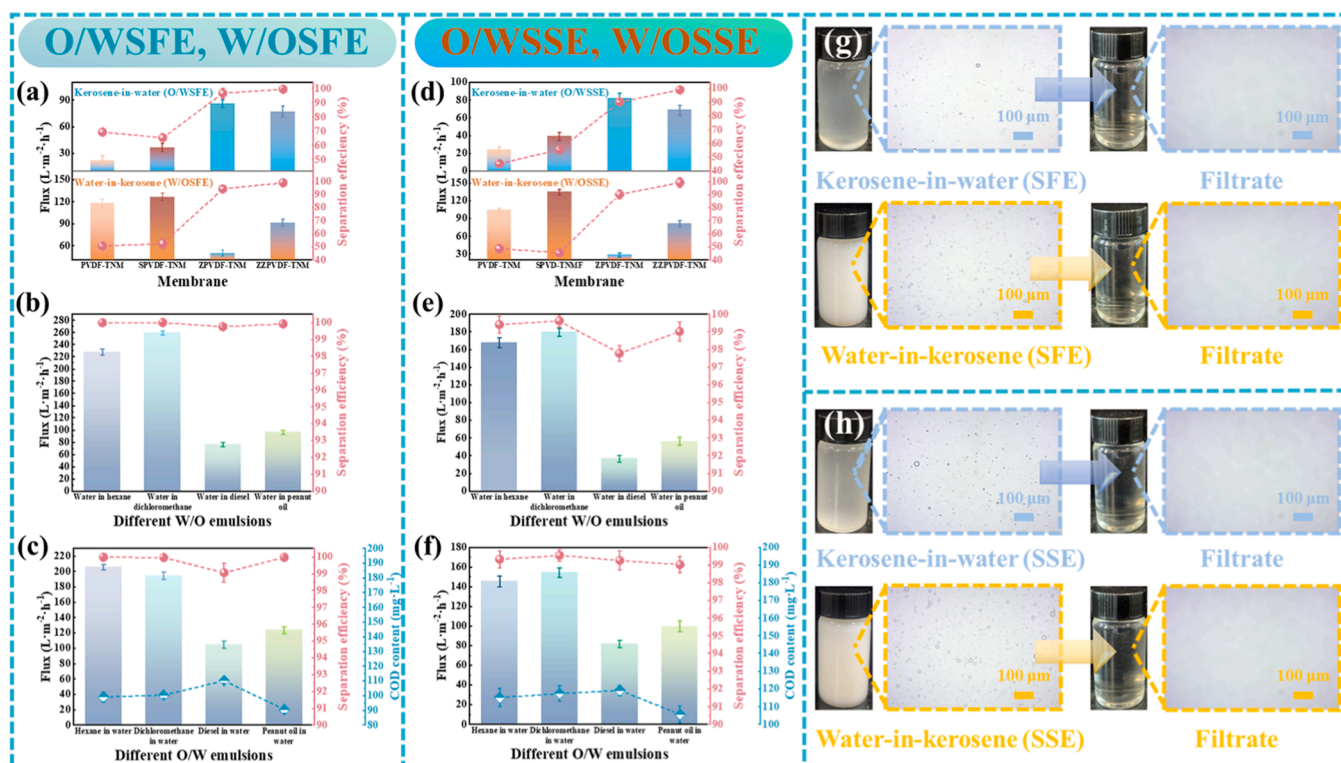
Fig. 7. Flux and separation efficiency of as-prepared membranes for (a) surfactants-free and (d) stabilized emulsions (kerosene-in-water, upper inset; and water-in-kerosene emulsions, lower inset); flux and separation efficiency of ZZPVDF-TNM for different (b) surfactants-free and (e) stabilized W/O emulsions; flux, separation efficiency and COD content in filtrates of ZZPVDF-TNM for (c) different surfactants-free and (f) stabilized O/W emulsions; (g) digital and (h) optical microscopic photographs of emulsions before and after separation by ZZPVDF-TNM.

the wetting configurations are analyzed to clarify the unique wetting properties of as-prepared ZZPVDF-TNM [67]. When a membrane surface is wetted by the first liquid (liquid I), the wetting behavior of the second liquid (liquid II) at the membrane surface also can be explained by the Young's equation, Eq. (5) [68]:

$$\cos\theta_{I-II} = \frac{\gamma_I\cos\theta_I - \gamma_{II}\cos\theta_{II}}{\gamma_{I-II}}\# \tag{5}$$

here, θ_I, θ_{II} and θ_{I-II} stand for the intrinsic contact angle of liquid I, liquid

II, and liquid I on liquid II in air; γ_I, γ_{II} and γ_{I-II} are the surface intension of liquid I-air, liquid II-air, and liquid I-liquid II, respectively.

As the ZZPVDF-TNM is super-amphiphilic in air, which means that both of θ_I and θ_{II} are 0°, thus $\cos\theta_I = \cos\theta_{II} = 1$. When the $\gamma_{II} > \gamma_I$, $\cos\theta_{I-II}$ will be less than 0 ($\gamma_{I-II} > 0$), thus θ_{I-II} must be over 90°, endowing the ZZPVDF-TNM an oil-repellent property underwater due to $\gamma_{water-air} > \gamma_{oil-air}$. Alternatively, Cassie-type wetting states for both water in oil and oil in water can be achieved by unique nanoarchitecture and appropriate surface chemical features, inducing the superamphiphobicity [49].
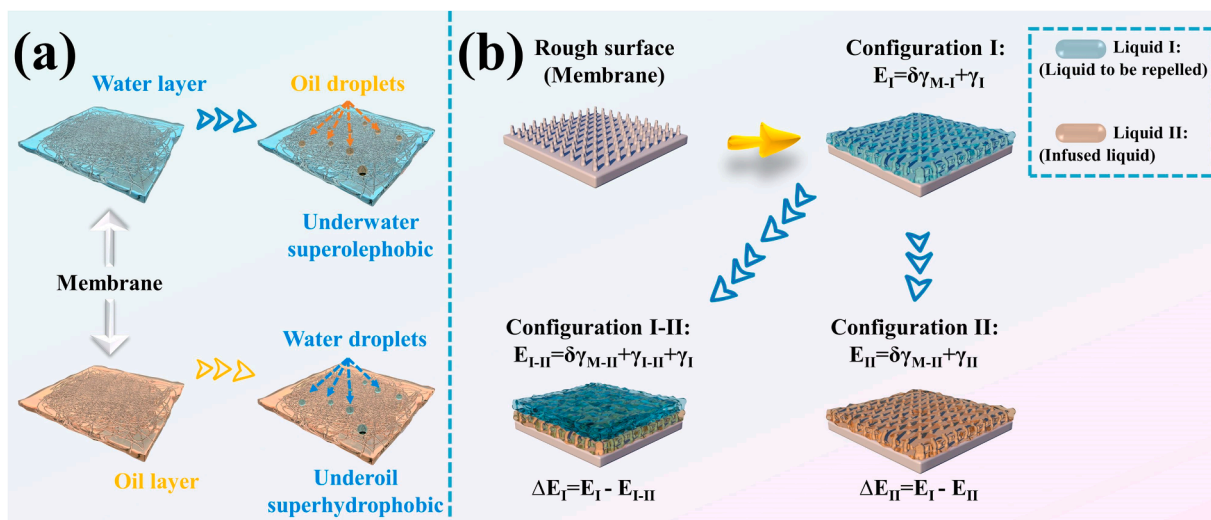

Fig. 8. (a) Schematic illustration of the controllable water/oil emulsion separation mechanism; (b) thermodynamic wetting models: configuration I and II represent the states that the membrane surface is sufficiently wetted by liquid I and II, respectively; configuration I-II represents the state that membrane surface is previously wetted by liquid II and makes liquid I float on it's top.

Based on the above analysis, it can be concluded that a stable liquid layer can be formed in the micro/nano rough structure of ZZPVDF-TNM's surface; meanwhile, the preferentially infiltrated liquid layer is firmly trapped and hardly replaced by other liquids, showing a stable under-liquid hydrophobic property (Fig. 8) [69]. Moreover, whether the membrane surface will be wetted by liquid I or liquid II depends on the total interfacial energy between the liquid and the membrane surface (solid) [70]. When the surface energies of liquid I and liquid II are different, the liquid with lower surface energy (E) always spreads the membrane surface preferentially [71,72] (the detailed calculations and analysis of ΔE can be found in section 1.8 of supplimentary information).

Take hydrophilic membrane for example, the separation mechanism of the membrane was further investigated. Traditional 2D membrane exhibits a thin oleophilic layer modified by the hydrophilic group decoration (hydrophilic modification). In the initial stage of emulsion filtration, the hydrophilic functional layer with oil repelling features forms at membrane-oil-water interface, avoiding oil phase entry. However, this barrier may be eroded by the continuous penetration of oils in emulsions. Compared with traditional 2D membrane surface (flat or flake surface), prepared 3D ZZPVDF-TNM owns the stacked and rough micro-nano structure, which endows the robust oleophobicity for emulsion separation (Fig. 9). The water droplets in O/W emulsions can be rapidly captured by the water prewetted ZIF-8 @ZnO layer to form an impregnable "water-barrier" to continually repel oil entry. In details, as the O/W emulsion permeation to "water-barrier" is going on, the contact probability between liquid film (i.e., "water-barrier") and continuous phase (water) is much higher than that of oil disperse phase. Therefore, when the water phase is continuously supplemented, the "water-barrier" will be constantly maintained. Additionally, in a long-term emulsion filtration, the small oil droplets blocked by membrane will collide and coalesce into a large oil droplet due to their own gravity and inertia. Owing to the underwater-superoleophobicity, the large oil droplet has a propensity to remain a spherical or quasi-spherical shape to reduce the surface tension. And the large oil droplets may spontaneously detach from membrane surface to form free oil due to $\rho_{oil} < \rho_{H2O}$. Alternatively, prepared ZZPVDF-TNM also can be used to filtrate W/O emulsions based on its superior underliquid superamphiphobicity. This case is also applicable to the above situation, unlike oils, the large water droplets are more likely settled down rather than floating due to their own gravity and super-hydrophobicity of oil prewetted membrane, promoting W/O emulsions separation.

Although a limited number of works have been devoted to developing the novel membranes used in on-demand separation of W/O or O/W emulsions, the separation transition (or wettability transition) still requires complex operation, high energy consumption (heat, electricity, light, etc.) and the risk of secondary contamination [73–76]. The surface wettability of the ZZPVDF-TNM can be achieved by simply pre-wetting the water or oil to switch wettability without any external field or chemical stimulation. ZZPVDF-TNM can easily separate different emulsions with a high separation efficiency. Moreover, the unique tubular structure and gravity-driven mode of oil/water separation further broaden the application of prepared membranes, showing a promising application prospect.

3.5. Photocatalytic removal of ZZPVDF-TNM to various organic pollutants

The photo response activities of prepared membranes are investigated by UV–vis DRS spectra. As shown in Fig. 10a, a comparatively narrow adsorption band in UV region from a little amount of Zn-based compound in both pristine PVDF-TNM and SPVDF-TNM is observed. After hydrothermal reaction, a conspicuous UV-light absorption edge appears at about 450 nm which can be associated to the strong light-harvesting capacity of ZnO nanowires. Interestingly, the band edge of the standard absorption spectrum of ZnO is about 380 nm [35], whereas the absorption band edge of ZPVDF-TNM in this study is significantly red-shifted. This is probably due to the needle-like structure of the rich ZnO nanowires, which facilitates the capture of the incident photons. For ZZPVDF-TNM, the adsorption band edge has been obviously expanded to the visible-light region (band edge at about ~ 710 nm), revealing that ZIF-8 @ZnO heterostructures further enhance visible light adsorption ability. The energy bandgap values can be estimated by Tauc equations (Eq. S1), E_g values derived from Tauc-plots are 3.06 eV and 2.98 eV for the ZPVDF and ZZPVDF-TNM, respectively (the inset of Fig. 10a). To clarify the accurate band structure, VB-XPS analysis of prepared membranes are also investigated in this study (Fig. 10b). The VB potential of ZZPVDF-TNM is 2.51 eV, calculated by Eq. S2, which is lower than that of ZPVDF-TNM (2.49 eV). Additionally, the CB levels of ZPVDF and ZZPVDF-TNM can be estimated by the empirical formula: $E_{CB} = E_{VB} - E_g$, E_{CB} values of -0.57 eV and -0.47 eV, respectively. ZZPVDF-TNM with $E_g = 2.98$ eV (labeled in Fig. 10a) shows a favorable UV–visible light-absorption ability for photocatalytic pollutants removal.

Zeta potentials of pristine PVDF and ZZPVDF-TNM are displayed in Fig. 10c. Obviously, PVDF-TNM possess negative charges with a downward trend in the pH range of 3–10, which can be ascribed to the intense negative charges of F element in ample C-F bonds [77]. Since the surface of ZIF-8 is rich in positive charges, the negative charges of PVDF
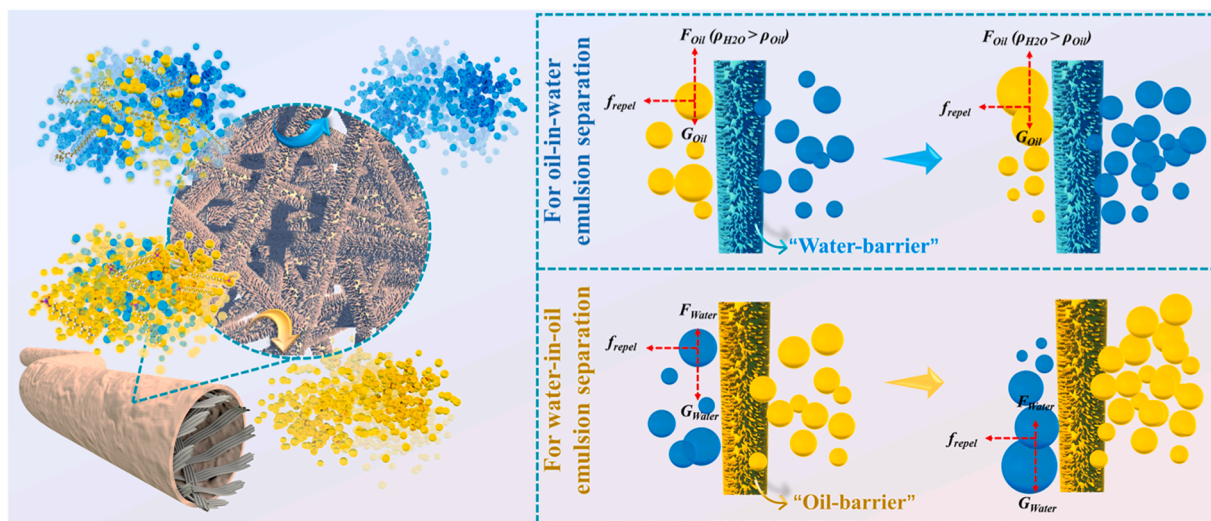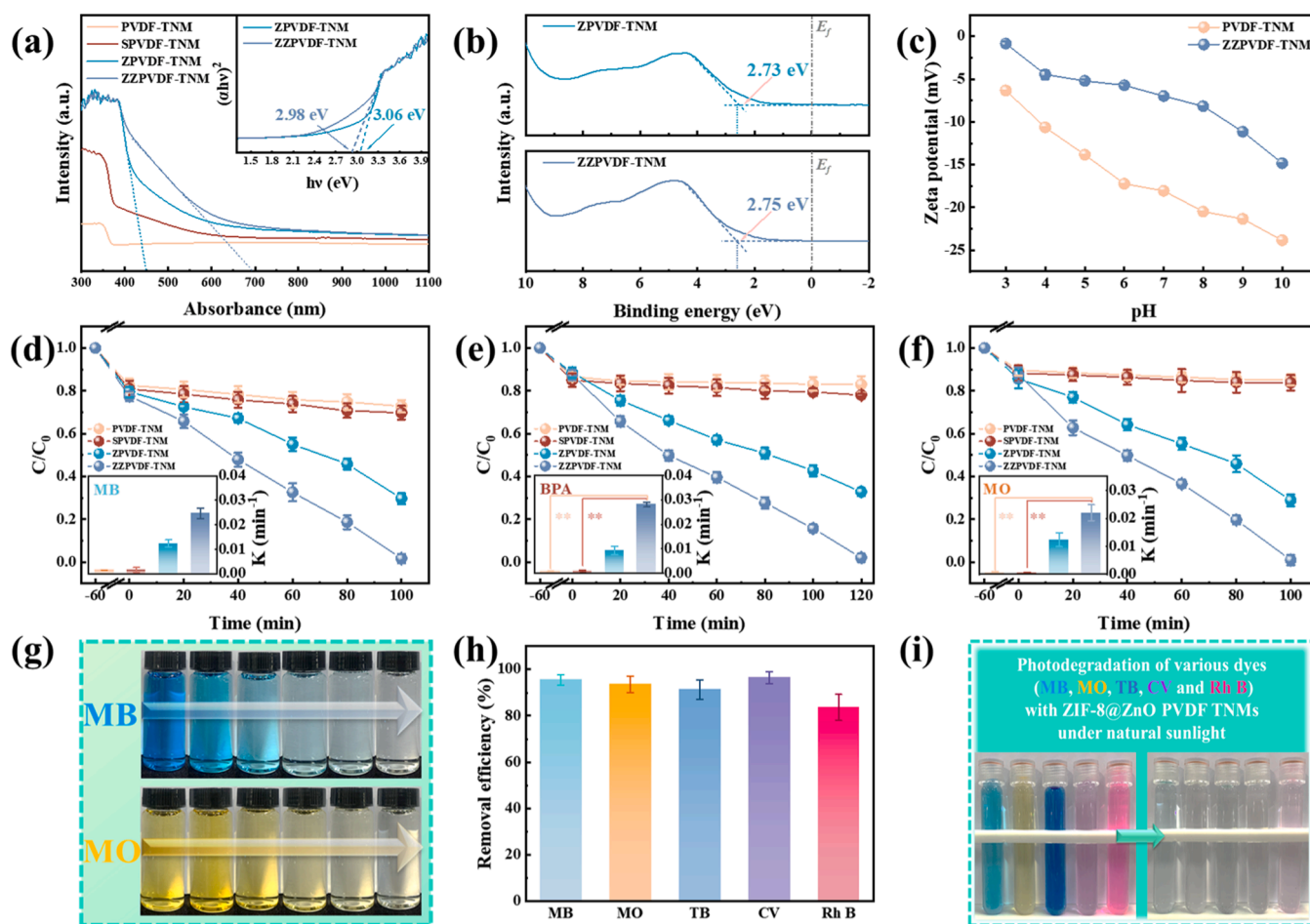

Fig. 9. Separation mechanism of as-prepared ZZPVDF-TNM for various emulsions.

Fig. 10. (a) UV–vis–DRS spectra of as-prepared membranes & Tauc plot of ZPVDF-TNM and ZZPVDF-TNM (the inset of a); (b) VB-XPS spectra and (c) Zeta-potential of ZPVDF-TNM and ZZPVDF-TNM; (d-f) contaminants removal efficiency of as-prepared membranes under simulated solar light catalysis ("**"means $P < 0.01$; i.e., highly significance); (g) photographs of MB and MO solution before and after photocatalysis; (h) photocatalytic removal efficiency and (i) optical images of ZZPVDF-TNM for various dyes (MB, MO, TB, CV and Rh B) under natural sunlight from 2 and 5 o'clock within 1 afternoon.

membrane will be weaken to some extent. The negative charges of ZZPVDF-TNM are less than that of PVDF-TNM in corresponding pH [78]. The reduced electronegativity of ZZPVDF-TNM will affect the adsorption of cationic pollutants, such as MB or deprotonated BPA molecules. Hence, the alkaline conditions are unrecommended for photocatalytic degradation of the positively charged pollutants.

Various soluble toxic substances (BPA, MB and MO) are chosen as the typical organic pollutants to evaluate the universal removal performance of prepared membranes (Fig. 10d-f). As expected, for different toxic substances, ZZPVDF-TNM possesses the highest photocatalytic performance compared to poor ZPVDF-TNM and the inert pristine PVDF-TNM. From the dynamic removal curves of prepared membranes, it is obvious that targeted pollutants can be removed within 120 min (Fig. 10 d-f). Moreover, it also can be described as the pseudo-first-order equation: $-ln (C/C_0) = kt$, where k (min^{-1}) and t (min) represent the photo-degradation rate constant and reaction time, respectively. As shown in inset of Fig. 10 d-f, the calculating constant of k values for BPA, MB and MO of ZZPVDF-TNM all exceed 0.02 min^{-1}, which is enhanced by 1.9 times compared to the ZPVDF-TNM ($k \approx 0.012$ min^{-1}). The decolorization of MB and MO solution intuitively demonstrates the excellent photocatalytic removal capacity for different toxic and stable dyes of ZZPVDF-TNM (Fig. 10g). Furthermore, ZZPVDF-TNM also shows admirable photocatalytic removal efficiency ($> 85\%$) for various toxic dyes including MB, MO, TB, CV and Rh B under natural sunlight irradiation (Fig. 10 h-i).

Various inorganic anions usually exist in actual wastewater, which

might have a negative effect on photocatalytic reaction. The effect of inorganic anions (CO$_3^{2-}$, NO$_3^-$, Cl$^-$ and SO$_4^{2-}$) on photocatalytic performance for BPA of ZZPVDF-TNM is analyzed here. As shown in Fig. 11a, there is an extremely slight drop in BPA removal efficiency after addition of CO$_3^{2-}$, indicating CO$_3^{2-}$ have a gentle impact on catalytic reaction. In fact, CO$_3^{2-}$ can hydrolyze into HCO$_3^-$ and OH$^-$ in aqueous solution, causing an increased pH value, which produces the negative effect as mentioned in Zeta potential [79]. On the other hand, CO$_3^{2-}$ can scavenge an extremely small amount of·OH to generate carbonate radicals (CO$_3^{·-}$) that possess a lower oxidation capacity (oxide potential, 1.57 ± 0.03 V vs. SHE) than that of·OH. Simultaneously, the reaction results in the increase of the pH value of the system (from 6.95 to 7.68), which is detrimental to photocatalytic activity [86]. With addition of NO$_3^-$, BPA removal efficiency also decreases gently, which can be attributed to the capture of photogenerated holes by NO$_3^-$. SO$_4^{2-}$ and Cl$^-$; and they are always employed to trap the holes and hydroxyl radicals in aqueous environment, so the photocatalytic BPA removal efficiency is also suppressed to some extent [80]. In detail, the BPA removal efficiencies of ZZPVDF-TNM with addition of these inorganic ions decrease in the order of SO$_4^{2-}$ > Cl$^-$ > NO$_3^-$ > CO$_3^{2-}$, demonstrating that it is not recommended for purification of the wastewater containing such ions with high concentration.

As shown in Fig. 11b, after enduring 10 cycles of photocatalytic BPA removal reaction, the ZZPVDF-TNM maintains a favorable stability and recyclability, demonstrating the membrane could act as a stable photocatalytic membrane for water purification. For metal-based catalysts
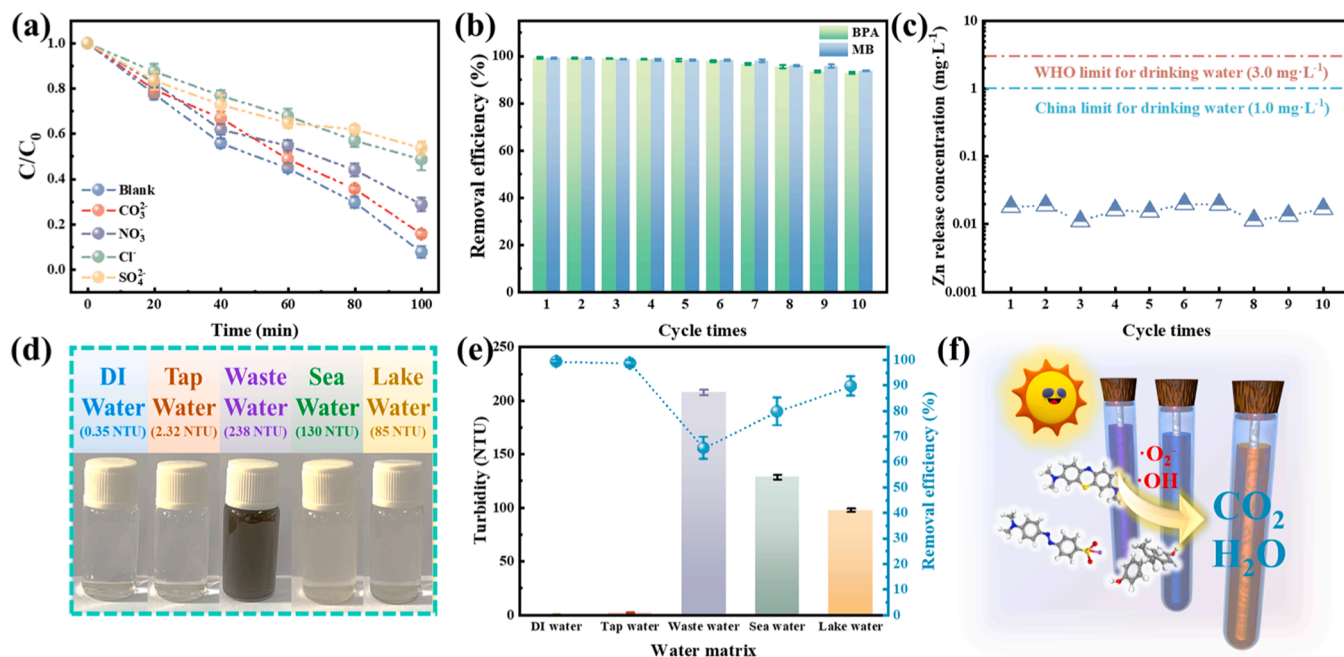
Fig. 11. (a) Effect of inorganic anions on BPA photocatalytic removal and (b) reusability of ZZPVDF-TNM; (c) leachability of Zn ions during 10 times photocatalysis cycles; (d) photographs of various water matrices; (e) turbidity and photocatalytic removal efficiency of various water matrices by ZZPVDF-TNM; (f) schematic diagram of ZZPVDF-TNM with various water matrices for pollutants photocatalysis.

used in wastewater treatment, the leachability of metal ions as a critical index should be concerned. Here, the leachability of Zn^{2+} for ZZPVDF-TNM after photocatalysis is determined by ICP-OES test. As shown in Fig. 11c, the accumulated concentration of Zn^{2+} at the end of each cycle test keep a low level of 0.01–0.026 mg·L^{-1}, which is far below the level of China and WHO regulations (0.1 and 0.3 mg·L^{-1}, respectively).

The effects of various water matrices on photocatalytic BPA removal efficiency for ZZPVDF-TNM are further investigated. As shown in Fig. 11d, the turbidity of DI water and tap water is remarkably low (0.35 NTU for DI water, 2.32 NTU for tap water, respectively), and they are clear and transparent. However, the turbidity of the actual wastewater is up to 237.56 NTU with a dark emulsion-like appearance. The actual seawater also possesses a high turbidity of 129.80 NTU due to the abundance of various dregs, dust and other particles, followed by the turbidity of 85.27 NTU for lake water. As illustrated in Fig. 10e, the BPA photocatalytic removal efficiency of ZZPVDF-TNM in DI water, tap water, actual wastewater, sea water and lake water are 99.27%, 97.56%, 65.35%, 79.64% and 89.64%, respectively. Obviously, the pollutant removal efficiency follows a decreasing trend with the increased turbidity. Even if that's the case, though, ZZPVDF-TNM still exhibits commendable performance to various water matrices (Fig. 11f).

In order to elucidate the photocatalytic BPA degradation mechanisms of ZZPVDF-TNM, the intermediate products are detected by high-resolution GC-MS. The entire MS spectra in BPA degradation process at different reaction time intervals (0, 60 and 120 min) are displayed in Fig. 12a-c. It is clearly that the peak intensity of BPA ($m/z = 228$) gradually decreases with the increased irradiation time. Briefly, the signal peaks of small molecule substances with m/z in the range of 50–200 appear and then fade, indicating the BPA molecules have been photodegraded into small molecule products. DFT calculation is employed to analyze the frontier molecular orbitals and predict the reaction sites for active sites during the BPA photocatalysis [81,82]. The molecular structure, highest occupied molecular orbital (HOMO) and lowest unoccupied molecular orbital (LUMO) of BPA molecules are presented in Fig. S5. Apparently, the HOMO orbital is mainly located at both sides as the density of HOMO distribution moves from center to sides at hydrogen atoms in phenolic ring groups, whereas the LUMO

orbital is mostly situated at the center situation involving in phenolic groups and hydrocarbons [83]. Based on Fukui function theory, the reaction activity is closely relative to Fukui index values [84,85]. A high f^- value indicates that the atom is more easily attacked by electrophilic reagent, while a high f^+ value demonstrates the atom is susceptible to nucleophilic attack, and a high value of f^0 means that the atom is vulnerable to be attacked by radicals [86]. As listed in Table S1, the f^- values of C^1, C^2, C^{12}, C^{13}, O^{16} and O^{17} are higher than other atoms, demonstrating the potential for attack and oxidation of h$^+$. And the C^2, C^3, C^6, C^{11}, C^{12} and C^{14} possess the higher f^+ values, which indicates that these atoms will be easily attacked by·O$_2$. High f^0 positions (such as C^2, C^3, C^6, C^{11}, C^{12}, O^{16} and O^{17}) suggest that these sites can be easily destructed by·OH. Various bond order such as Wiberg bond order (WBO), Laplacian bond order (LBO) and Fuzzy bond order (FBO) and Fukui function analysis were employed to predict the reactivity, stability and fracture behavior of BPA molecules as shown in Fig. 12d-f. [87,88]. It is obviously that the bond orders of C^4-C^7 (bond 7) and C^7-C^{10} (bond 10) are the lowest, demonstrating that they are most likely to be broken after being attacked by these reactive species [83].

In view of DFT analysis and GC-MS results, a possible degradation pathway of BPA molecules is proposed as depicted in Fig. S6. After the fracture of bond 7 and 10, the hydroxy-bonded C (C^1 or C^{13}) of BPA is first attacked by the electrophilic attack by h$^+$, causing the dihydroxylation labelled as P1 production. Subsequently, P1 can be oxidized into p-phenol (P2); P2 is attacked by different free radicals to form phenol (P3) or P4 after ring-opening reaction [89]. Specifically, C^2 and C^{12} sites of BPA can be directly attacked by·OH or·O$_2$ to form a multi-hydroxylation substance, P5. Further, the BPA molecules can be oxidized to P6 and P7 with attacking of·OH, and the C-C bonds between isopropyl and benzene rings will rupture and be oxidized by various radicals [90]. Ultimately, aromatic compounds in BPA transform into ring-opened intermediates and are mineralized into harmless small molecules and nontoxic substances, H$_2$O and CO$_2$. And the intermediates generated in BPA photo-degradation in this study has also been confirmed in previous reports [89,91,92].

In order to further investigate the toxicity of the intermediates during BPA degradation, the T.E.S.T. based on QSAR mathematical models
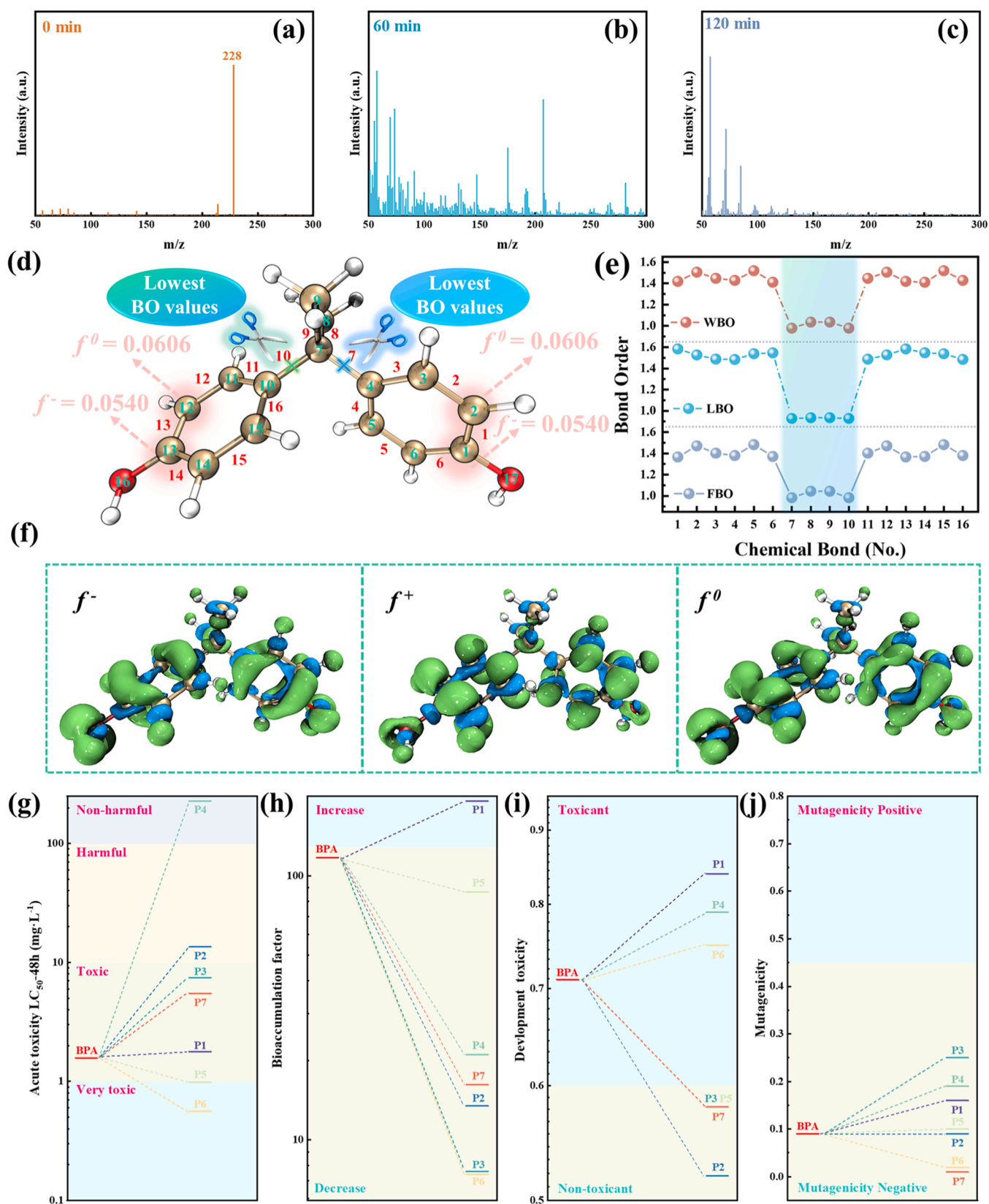
Fig. 12. (a-c) Mass spectra of BPA at 0, 60 and 120 min after photocatalytic degradation by ZZPVDF-TNM; (d) schematic illustration of reactive sites of BPA molecules calculated by bond orders and Fukui function; (e) bond order (WBO, LBO and FBO) and (f) Fukui index isosurface (f^-, f^+ and f^0) of BPA molecule; (g) acute toxicity LC$_{50}$-48 h (Daphnia magna), (h) bioaccumulation factor, (i) development toxicity and (j) mutagenicity of BPA and its degradation intermediates after ZZPVDF-TNM photocatalysis.

is performed to evaluate the acute toxicity [93,94]. As depicted in Fig. 12 g, the acute toxicity of BPA and its intermediates can be reflected by the lethal concentration of Daphnia magna (LC_{50}-48 h). Obviously, the acute toxicity LC_{50} value of BPA is 1.73 mg·L^{-1}, which can be considered as "toxic" category. With the exception of P5 and P6, the acute toxicity LC_{50} value of other intermediates increases to some extent, indicating that the toxicity gradually decreases due to the attack of reactive species. According to the bioaccumulation factors (Fig. 12 h) of all intermediates with the exception of P1 are significantly lower than pristine BPA, showing a trend from "Increase" to "Decrease". This trend also follows a similar pattern with the acute toxicity of Daphnia magna (LC_{50}-48 h), demonstrating that the bioaccumulation toxicity of these intermediates is comparatively decreased with photocatalysis of ZZPVDF-TNM. As shown in Fig. 12i, although the developmental toxicities of a few of intermediates are slightly higher than that of BPA, the degradation products will gradually transfer into "non-toxicant" substances with the sequential oxidations by·OH,·O_2^- and h^+. As depicted in Fig. 12j, both BPA and its intermediates have low mutagenicity, indicating that ZnO@ZIF-8 photocatalysis system is safe and hardly affects on the mutagenicity of BPA. All of above toxicity indexes illustrate that ZZPVDF-TNM can realize the gradual detoxification of BPA step-by-step. Sometimes, the acute toxicity of some intermediates is equivalent or higher than pristine BPA, which means that the thorough photo-degradation process should be carried out to improve the ecosystem safety and water quality [95,96]. Overall, the ultimate toxicity of all intermediates is considerably low, suggesting that the ZZPVDF-TNM possess a high bio-safety and environment-friendliness for wastewater purification.

In the active species trapping experiment, 2 mM of various additives including TBA, BQ and EDTA-2Na are regarded as quenchers of·OH,·O_2^- and h^+, respectively. As displayed in Fig. 13a, an 99% of BPA photodegradation rate can be achieved under simulated sunlight irradiation without any scavengers. After addition of TBA, BQ, EDTA-2Na and *L*-HIS, the photodegradation rate of BPA drops to 64.58%, 60.57%, 71.58% and 97.26% (keeping relatively constant), respectively. Notably, there is no significant decrease in photodegradation of BPA after *L*-HIS addition, indicating no generation of $^1O_2$ in the system. This

reveals that·OH and·O_2^- are the main active species and h^+ plays a minor role in photocatalysis. EPR spectra are further performed to confirm the main active species during photocatalytic process. As presented in Fig. 13b, no signals of DMPO-·OH, DMPO-·O_2^- and TEMP-$^1O_2$ can be detected in dark. After irradiation for 10 min, the signals of DMPO-·OH and DMPO-·O_2^- are clearly observed with an intensity ratio of 1:2:2:1 and 1:1:1:1 of four peaks, respectively. However, no signal of TEMP-$^1O_2$ (a triplet peak with the intensity ratio of 1:1:1) after irradiation can be detected. These signals also prove that·OH and·O_2^- are the key active species in photocatalytic reaction.

In another fluorescence test, as shown in Fig. 13c, no obvious fluorescence signal peak can be detected in bare TA reaction solution. After the simulated sun light irradiation, for both PVDF-TNM+TA solution and SPVDF-TNM+TA solution, there are the faint signals generated by the reaction of·OH radicals and TA. In comparison, an exceptionally intensive fluorescence signal peak appears in ZZPVDF-TNM+TA solution, which demonstrates there are a supply of·OH radicals which can oxidize TA to a highly fluorescent hydroxyterephthalate (TAOH) [97].

The results of photoluminescence (PL) emission can indirectly reflect the transfer, migration and recombination of photogenerated charge carriers. PL spectra and TRPL spectra are employed to qualitatively evaluate the photogenerated carriers' separation of membranes. As shown in Fig. 13d, a relatively intensive emission peak can be detected in ZPVDF-TNM, demonstrating a large number of photogenerated carriers have recombined and annihilated. In comparison, the peak intensity of ZZPVDF-TNM is obviously lower than that of ZPVDF-TNM, which indicates the less recombining probability of charge carriers and high photocatalytic activity. Additionally, from TRPL spectra in Fig. 13e, the average lifetime of photogenerated charge carriers of ZZPVDF-TNM is 1.1025 ns, which is longer than that of ZPVDF-TNM with the value of 0.9070 ns. This confirms an efficient electron-hole pairs separation and positive charge transfer capability in ZZPVDF-TNM [87]. The charge density difference of ZnO and ZIF-8 is depicted in Fig. 13f, where the yellow and cyan regions represent charge's accumulation and depletion, respectively. Obviously, the photogenerated electrons migrate from ZIF-8 to ZnO, resulting in the accumulation of photogenerated charges on the interface, which is consistent
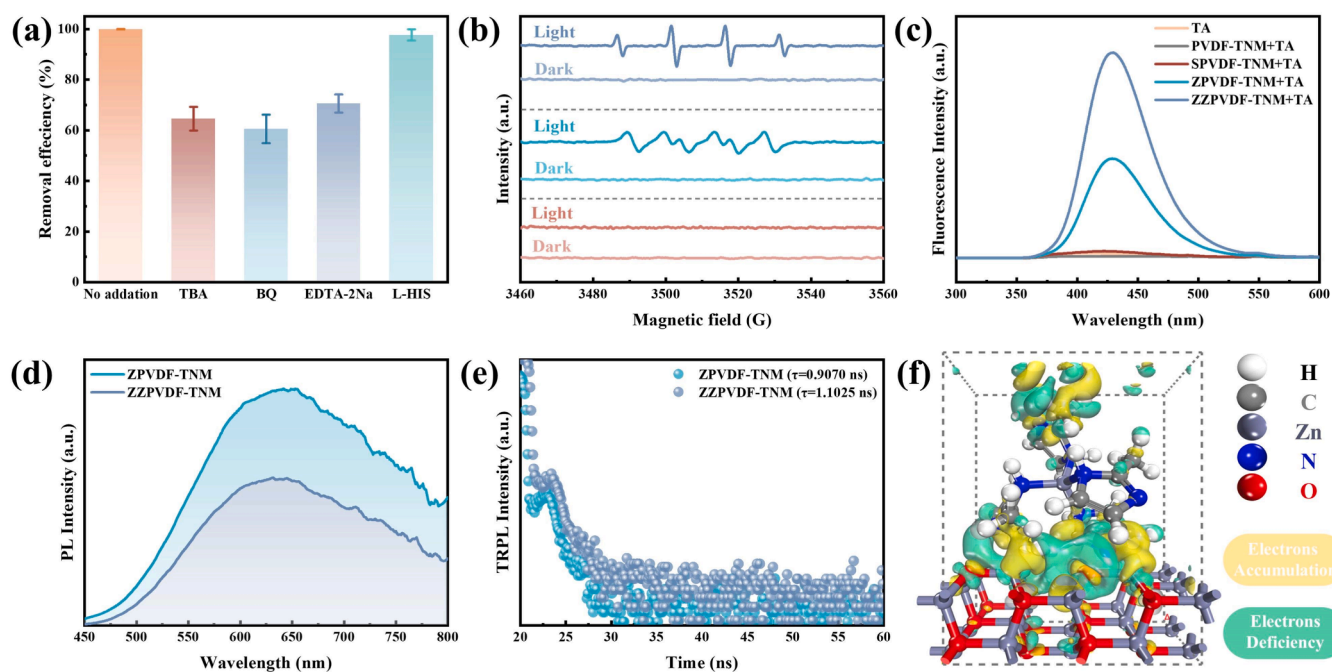
Fig. 13. (a) BPA removal efficiency of ZZPVDF-TNM with different quenchers under solar light illumination; (b) EPR signals for DMPO-·OH, DMPO-·O_2^- and TEMP-$^1O_2$; (c) fluorescence emission spectra; (d) PL and (e) TRPL spectra of ZPVDF-TNM and ZZPVDF-TNM; (f) charge density difference of interface between ZIF-8 and ZnO heterojunction.
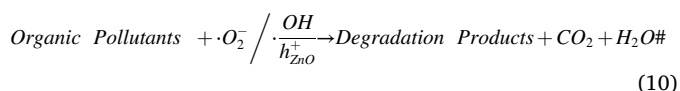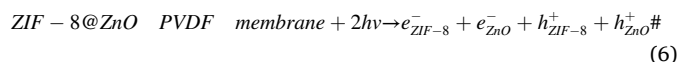
with above analysis and XPS results (Zn 2p signal) [98,99].

Based on aforementioned analysis, a possible photocatalytic mechanism is proposed for pollutants degradation of ZZPVDF-TNM (Fig. 14). Under sunlight irradiation, the ZIF-8 @ZnO nanorods immobilized on ZZPVDF-TNM will be excited to generate electrons and holes. It is well known that both ZnO and ZIF-8 are *n*-type of semiconductors; therefore a "*n-n*" type of heterojunction system can be formed after intimate combination (Fig. 14a & b) [100]. Specifically, the CB level of − 0.57 eV and VB level of 2.49 eV of ZnO are lower than those of ZIF-8 (E_{CB}= −3.40 eV, E_{VB}=1.60 eV), when excited by light, the electrons constantly move from ZIF-8 to ZnO until the Fermi levels become coincident [101]. A space charge region can be formed between the two interfaces, and the band bending of ZnO and ZIF-8 happens. The energy band of ZIF-8 will bend upward due to loss of electrons, whereas the energy band of ZnO will bend down due to accumulation of electrons. In this process, a built-in electric field (IEF) can be formulated where the electron transfer at the interface between ZIF-8 and ZnO reaches equilibrium, which plays a positive role in the separation of photogenerated electrons and holes [87,99,102].

According to above analysis,·OH and·O$_2^-$ are the dominant active species in photocatalysis of ZZPVDF-TNM with solar light irradiation. If it is assumed that the electron transfer path of the membrane followed Type-II mechanism (Fig. 14c), water molecules will be unable to be oxidized to·OH since E_{VB}= 1.60 eV of ZIF-8 is more negative than that of the redox potential of·OH/H$_2$O (2.27 eV vs. NHE) [103]. Therefore,·OH can be generated only when the electron transfer pathway follows Z-Scheme (Fig. 14d). Z-Scheme ZnO@ZIF-8 heterojunction promote the electrons transport and electron-hole pairs separation, enhancing the photocatalytic pollutant removal efficiency of prepared membranes. Here, the ZZPVDF-TNM possess more negative CB potential (−0.47 eV) than the standard redox potential of O$_2$/·O$_2^-$ (−0.33 eV vs. NHE) [87];

and more positive VB potential (2.51 eV) than the standard redox potential of·OH/H$_2$O (2.27 eV vs. NHE), so that electrons in CB of ZIF-8 and holes in VB of ZnO can respectively react with adsorbed O$_2$ and H$_2$O to generate·O$_2^-$ and·OH. The·O$_2^-$,·OH and h$^+$ produced during in photocatalytic process can participate directly in photodegradation of various organic pollutants including drugs, dyes and oils [103]. The main reactions are listed as the following equations:

$$ZIF-8@ZnO \quad PVDF \quad membrane + 2hv \rightarrow e^-_{ZIF-8} + e^-_{ZnO} + h^+_{ZIF-8} + h^+_{ZnO} \#$$
(6)

$$e^-_{ZnO} + h^+_{ZIF-8} \rightarrow recombination \#$$
(7)

$$e^-_{ZIF-8} + O_2 \rightarrow \cdot O_2^- \#$$
(8)

$$h^+_{ZnO} + H_2O \rightarrow \cdot OH + H^+ \#$$
(9)

$$Organic \quad Pollutants \quad + \cdot O_2^- \Big/ \frac{\cdot OH}{h^+_{ZnO}} \rightarrow Degradation \quad Products + CO_2 + H_2O \#$$
(10)

3.6. Antifouling performance and membrane regeneration

Here, the multi cyclic emulsions separation are operated to evaluate the antifouling performance of prepared membranes. As depicted in Fig. 15a, the filtration flux of O/WSFE maintains at > 60 L·m^{-2}·h^{-1}, and the separation efficiency of emulsions is still up to 99.0% after 10 cycles. And the flux of O/WSSE is also maintained at a stable level (> 50 L·m^{-2}·h^{-1}) with a high separation efficiency (> 98.3%) after 10 cycles. As shown in Fig. 15b, it also exhibits a remarkable separation ability for W/OSFE (filtration flux is more than 84.5 L·m^{-2}·h^{-1} with
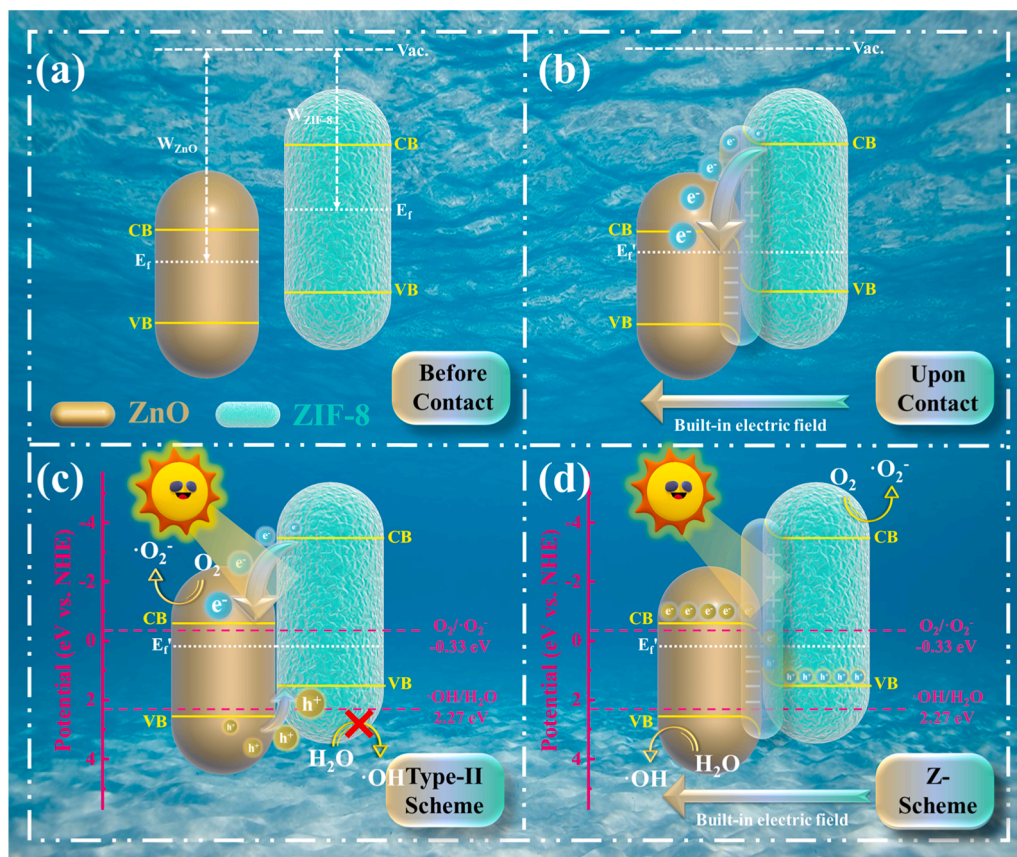
Fig. 14. Schematic illustration of photocatalytic mechanism of ZIF-8 @ZnO-PVDF tubular nanofiber membrane: (a) before contact; (b) upon contact; (c) scheme of Type-II heterojunction; (d) scheme of Z-type heterojunction.
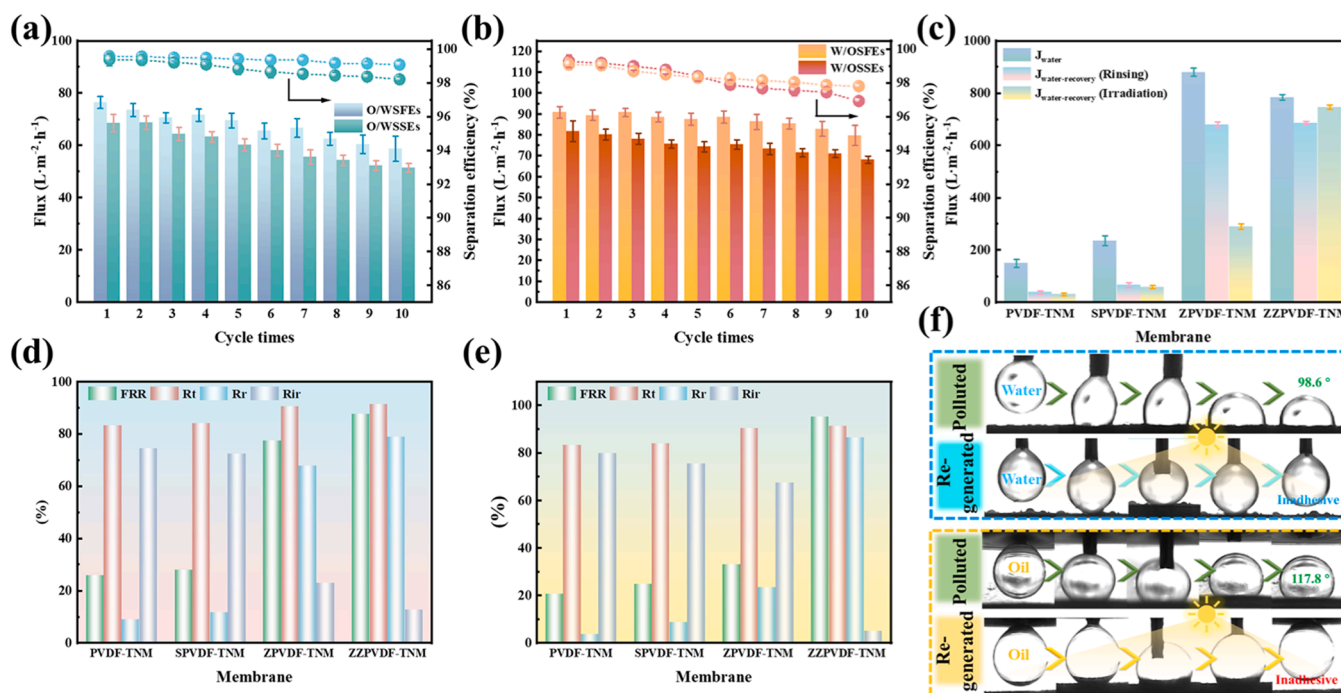
Fig. 15. Cyclic separation performance of ZZPVDF-TNM for (a) oil-in-water and (b) water-in-oil emulsions; (c) water flux of ZZPVDF-TNM in four-step of continuous filtration tests (water-emulsion-water-water); fouling indexes (FRR, Rt, Rr and Rir) of as-prepared membranes for (d) hydraulic cleaning and (e) photocatalytic self-cleaning; (f) UOWCA and UWOCA after fouling by emulsions and subsequent regeneration by photocatalytic self-cleaning and hydraulic cleaning.

separation efficiency more than 98%) and W/OSSE (filtration flux is 71.3 L·m^{-2}·h^{-1} with separation efficiency more than 96.5%).

In terms of different cleaning methods of membrane generation containing ordinary hydraulic cleaning and photocatalytic self-cleaning, as shown in Fig. 15c, photocatalytic self-cleaning is a preferred method for the filtration flux recovery. In the four-step of continuous filtration tests, the corresponding FRRs of PVDF, SPVDF, ZPVDF and ZZPVDF-TNM after hydraulic cleaning are calculated as 25.67%, 27.63%, 77.22% and 85.43%, respectively (Fig. 15d). Obviously, the FRR value of ZZPVDF-TNM is much higher than that of the other membranes, demonstrating that ZIF-8 @ZnO nanorods with multi-scale nano-architecture exhibit an excellent anti-fouling with underwater low-oil-adhesion, which is consistent with the experimental findings of wettability. Encouragingly, as shown in Fig. 15e, the water flux of oil-contaminated ZZPVDF-TNM can be almost completely recovered after a period of solar light irradiation with a high FRR value of 95.11%, which is remarkably higher than those of pristine PVDF-TNM of 20.27%, SPVDF-TNM of 24.68% and ZPVDF-TNM of 32.80%. Furthermore, the ZZPVDF-TNM possess low Rir values (12.57% & 4.88% for hydraulic cleaning and photocatalytic self-cleaning) and high Rr values (78.62% & 86.31% for hydraulic cleaning and photocatalytic self-cleaning), demonstrating that prepared membranes are able to maintain a stable and robust filtration flux against the membrane fouling. As a photocatalytic recoverable membrane, the fouled membrane needs merely a period of light irradiation to fulfil self-cleaning recovery, showing great promise for complex wastewater remediation [52,104]. To investigate the photocatalytic self-cleaning capacity, UWOCA and UOWCA of fouled and regenerated ZZPVDF-TNM are also tested. As depicted in Fig. 15f, the fouled ZZPVDF-TNM shows a UOWCA of 98.6° and UWOCA of 117.8°, respectively. After regeneration by irradiation of simulated solar light, the underwater superoleophobicity and underoil super-hydrophobicity of the self-cleaning ZZPVDF-TNM can be recovered, showing excellent anti-adherence properties to oil (underwater) and water (underoil). In terms of the fouled ZZPVDF-TNM (contaminated by O/WSSE initially), the remnant oil droplets adhered on the membrane surface can be removed by the active species oxidation via

photocatalysis; and then a large number of water molecules can be captured by the rough hierarchical structure of ZIF-8 @ZnO nanorods to form a robust "water-barrier" layer to repel the oils. The same situation is also applicable to the generated membrane fouled by W/OSSE. The optical images of the polluted ZZPVDF-TNM after several times of MB photocatalysis and regenerated ZZPVDF-TNM removed by photocatalysis can be found in Fig. S7, intuitively displaying the contaminants' evolution and disappearing on membrane surface. In addition, prepared ZZPVDF-TNM hardly dissolved in DMAc/acetone due to the complete encapsulation of ZIF-8 @ZnO nanorods on membrane surface, demonstrating the fulfilling polar solvent resistance of ZZPVDF-TNM (Fig. S8).

3.7. Simultaneous removal of complex wastewater in "filtration + photocatalysis" mode

The actual oily wastewater is usually a complex system containing various ingredients such as insoluble oils and soluble pollutants (e.g., drugs, dyes, etc.). Treatment of the oily wastewater has become a tricky problem for oil/water separation membrane. Accordingly, a laboratory-scale continuous filtration system is constructed as displayed in Fig. 16a. Various complex emulsions have been used to evaluate the pollutants simultaneous removal capacity of ZZPVDF-TNM. As can be seen from Fig. 16b, the blue SFE and SSE with MB turns transparent, which further confirms that ZZPVDF-TNM possesses fast and admirable photocatalytic activity [105].

As shown in Fig. 16c & d, the removal efficiency for MB and BPA in emulsions of "filtration + photocatalysis" mode with ZZPVDF-TNM is obviously higher than that of filtration only, and the highest removal efficiency for MB, BPA and oil in surfactant free emulsion is 92.58%, 90.43% and 99.38%, respectively. The removal efficiency of surfactant stable emulsions (for MB, BPA and oil is 87.65%, 70.11% and 97.35%, respectively) experience a certain decrease, which may be ascribed to the hindrance effect of SSE solution on low light intensity. Clearly, the typical adsorption band of oils (~ 250 nm), BPA (278 nm) and MB (664 nm) in UV–vis spectra of surfactant-free and surfactant-stabilized
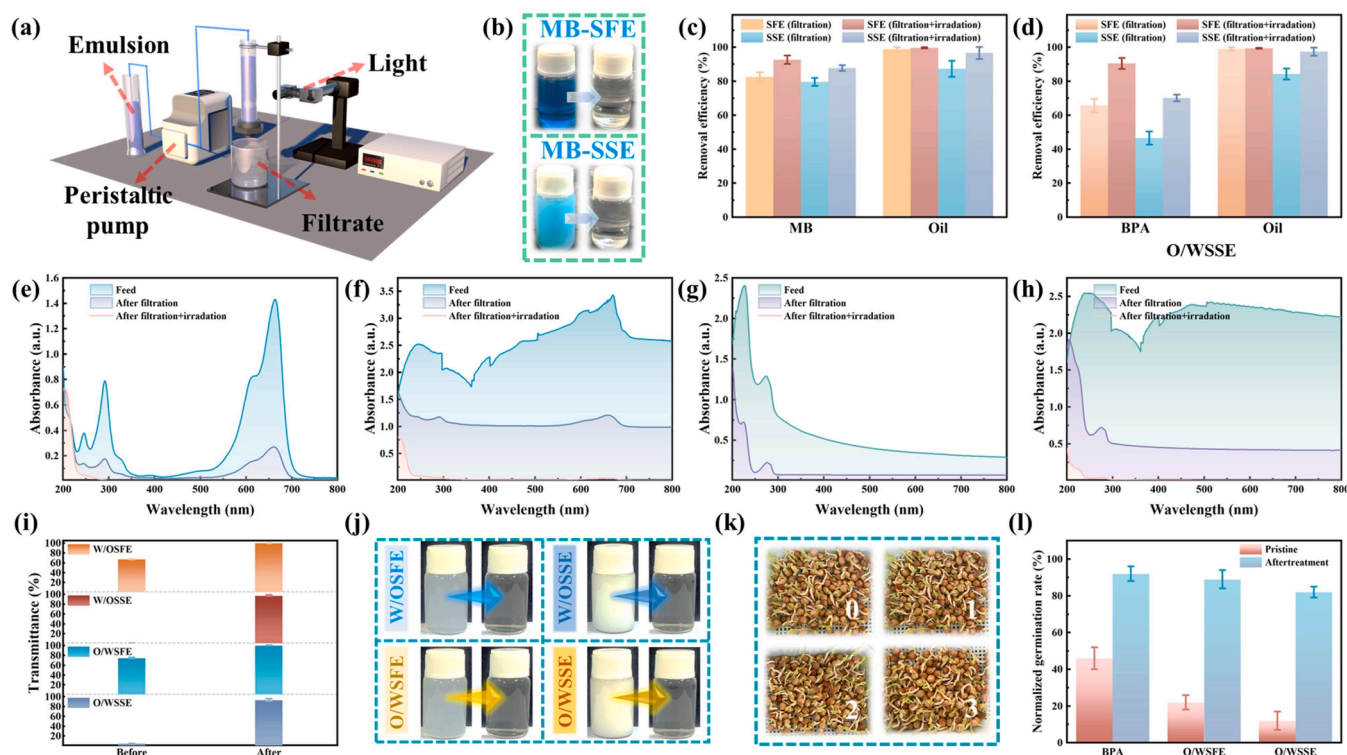
Fig. 16. (a) A lab-scale continuous filtration system coupled with Xeon-lamp using as-prepared ZZPVDF-TNM and (b) practical effects for MB in SFE/SSE; the removal efficiencies of (c) MB and (d) BPA in O/WSFE & O/WSSE in different filtration mode. UV–vis spectra of the feed, after filtration and filtration + irradiation of the hybrid complex emulsions: (e) MB in O/WSFE; (f) MB in O/WSSE; (g) BPA in O/WSFE; (h) BPA in O/WSSE; (i) the transmittance and (j) optical photographs of filtrates (filtration + irradiation) and feeding emulsions; (k) seed germination with tap water and filtrates, 0: with tap water; 1: with residual BPA solution after photocatalysis; 2: with filtrate after O/WSFE filtration; 3: with filtrate after O/WSSE filtration; (l) normalized germination rate with pristine and treated pollutant solution.

emulsions get flat and disappear, indicating that oils and pollutants have been removed simultaneously by prepared ZZPVDF-TNM (Fig. 16e-h). The filtrates of various SFEs after filtration or photocatalytic filtration is slightly higher than that of SSEs, demonstrating that most of impurities can be removed by ZZPVDF-TNM (Fig. 16i). The digital images show all of the filtrates are almost clear, indicating that ZZPVDF-TNM is competent in treating complex emulsions (Fig. 16j).

Furthermore, the seed germination experiment was carried out to evaluate the water quality after filtration or photocatalysis. As depicted in Fig. 16k & l, the normalized germination rate (G.P.), which is bred with BPA solution, O/WSFE and O/WSSE, is extremely low with the value of 46%, 22% and 12%, respectively. It is evident that BPA wastewater exhibited significant inhibition of germination for seeds, which is probably due to the suppression of the mitosis and photosynthesis of plants when the concentration of BPA exceeds 5 ppm [106]. In addition, the inhibition of seed germination by oily wastewater is mainly caused by the destroy of low-molecular hydrocarbons to cell membranes and the negative effect of the metabolism of seeds as well as the blockage of stomata, transpiration and respiration of plants by thin oil film formed by large molecular hydrocarbons [107]. Encouragingly, the G.P. rate of the seeds bred with BPA solution after photocatalysis, filtrated O/WSFE solution and filtrated O/WSSE solution are as high as 92.0%, 89.0% and 82.0%, respectively. It can be attributed to that most of the harmful substances such as drugs and oils have been successfully removed by the catalytic and filtration of prepared membranes. The purification of different complex wastewater by ZZPVDF-TNM is favorable for ecological recovery.

4. Conclusion

In summary, a caterpillar-inspired ZZPVDF-TNM with favorable solar light-driven photocatalytic activity was developed for efficiently wastewater purification and on-demand emulsions separation. Highly crystalline ZIF-8 @ZnO nanorods were anchored on the nanofibrous networks via hydrothermal and self-template scarifying method. The membrane surface with switchable wettability can be transformed between underwater superoleophobicity and underoil superhydrophobicity by simple wetting, showing superbly selective wettability for on-demand oily wastewater purification. In addition, the dense anchored ZIF-8 @ZnO nanorods act as a commendable multifunctional layer, which endows the ZZPVDF-TNM with a remarkable catalytic performance and anti-fouling ability for long-term filtration. As anticipated, the prepared membranes demonstrate an excellent filtration performance for various complex emulsions by only gravity-driven mode. The filtration flux and separation efficiency of O/W or W/O emulsions can be up to 258.4 L·m^{-2}·h^{-1} and ~ 99.9%. Moreover, the ZZPVDF-TNM exhibits an admirable photocatalytic removal capability of various soluble toxic pollutants (i.e., BPA, MB and MO) and insoluble oil droplets adhered to the membrane surface. The contaminated ZZPVDF-TNM can be nondestructively regenerated by solar light irradiation. Thus, our work may provide a strategy for developing the next-generation multifunctional membranes with favorable separation efficiency, permeability, anti-fouling and self-cleaning properties in waste water environment remediation such as the purification of oily wastewater with dyes, drugs, and other organic pollutants.

CRediT authorship contribution statement

Hongwei Piao: Draft writing, data analysis, conceptualization and review. **Jian Zhao:** Conceptualization, data analysis & writing. **Yifei Tang:** Data-colleting. **Run Zhang:** Data collecting. **Shujie Zhang:** Reviewing. **Qinglin Huang:** Revise, review. **Yong Liu:** Review. **Shiwei Zuo:** Review. **Changfa Xiao:** Review, editing. **Shaomin Liu:** Review, revise, editing.

Declaration of Competing Interest

The authors declare that they have no known competing financial interests or personal relationships that could have appeared to influence the work reported in this paper.

Data Availability

No data was used for the research described in the article.

Appendix A. Supporting information

Supplementary data associated with this article can be found in the online version at doi:10.1016/j.apcatb.2023.123300.

References

[1] L. Li, Z. Hu, J.C. Yu, On-demand synthesis of H_2O_2 by water oxidation for sustainable resource production and organic pollutant degradation, Angew. Chem. Int. Ed. 59 (2020) 20538–20544.

[2] X. Yang, H. Sun, G. Li, T. An, W. Choi, Fouling of TiO_2 induced by natural organic matters during photocatalytic water treatment: Mechanisms and regeneration strategy, Appl. Catal. B. 294 (2021) 120252.

[3] N. Sreedhar, M. Kumar, S. Al Jitan, N. Thomas, G. Palmisano, H.A. Arafat, 3D printed photocatalytic feed spacers functionalized with β-FeOOH nanorods inducing pollutant degradation and membrane cleaning capabilities in water treatment, Appl. Catal. B. 300 (2022), 120318.

[4] Y. Yang, S. Qiao, J. Zhou, X. Quan, A novel porous-carbon-based hollow fiber membrane with electrochemical reduction mediated by in-situ hydroxyl radical generation for fouling control and water treatment, Appl. Catal. B. 255 (2019), 117772.

[5] Z. Shi, H. Zeng, Y. Yuan, N. Shi, L. Wen, H. Rong, D. Zhu, L. Hu, L. Ji, L. Zhao, X. Zhang, Constructing superhydrophobicity by self-assembly of SiO_2@ polydopamine core-shell nanospheres with robust oil-water separation efficiency and anti-corrosion performance, Adv. Funct. Mater. 33 (2023) 2213042.

[6] H.M. Hegab, P. Kallem, R.P. Pandey, M. Ouda, F. Banat, S.W. Hasan, Mechanistic insights into the selective mass-transport and fabrication of holey graphene-based membranes for water purification applications, Chem. Eng. J. 431 (2022), 134248.

[7] C. Chen, M. Wang, X. Chen, X. Chen, Q. Fu, H. Deng, Recent progress in solar photothermal steam technology for water purification and energy utilization, Chem. Eng. J. 448 (2022), 137603.

[8] S. Xiao, X. Huo, Y. Tong, C. Cheng, S. Yu, X. Tan, Improvement of thin-film nanocomposite (TFN) membrane performance by CAU-1 with low charge and small size, Sep. Purif. Technol. 274 (2021) 118467.

[9] S. Xiao, X. Huo, S. Fan, K. Zhao, S. Yu, X. Tan, Design and synthesis of Al-MOF/ PPSU mixed matrix membrane with pollution resistance, Chin. J. Chem. Eng. 29 (2021) 110–120.

[10] S. Shi, Y. Si, Y. Han, T. Wu, M.I. Iqbal, B. Fei, R.K.Y. Li, J. Hu, J. Qu, Recent progress in protective membranes fabricated via electrospinning: advanced materials, biomimetic structures, and functional applications, Adv. Mater. 34 (2022) 2107938.

[11] Y. Li, S. Xiao, Y. Luo, S. Tian, J. Tang, X. Zhang, J. Xiong, Advances in electrospun nanofibers for triboelectric nanogenerators, Nano Energy 104 (2022), 107884.

[12] S. Zheng, H. Chen, X. Tong, Z. Wang, J.C. Crittenden, M. Huang, Integration of a photo-fenton reaction and a membrane filtration using CS/PAN@FeOOH/g-C$_3$N$_4$ electrospun nanofibers: synthesis, characterization, self-cleaning performance and mechanism, Appl. Catal. B. 281 (2021), 119519.

[13] A. Xie, Y. Wu, Y. Liu, C. Xue, G. Ding, G. Cheng, J. Cui, J. Pan, Robust antifouling NH$_2$-MIL-88B coated quartz fibrous membrane for efficient gravity-driven oil-water emulsion separation, J. Membr. Sci. 644 (2022), 120093.

[14] X. Lin, S. Xia, L. Zhang, Y. Zhang, S. Sun, Y. Chen, S. Chen, B. Ding, J. Yu, J. Yan, Fabrication of flexible mesoporous black Nb$_2$O$_5$ nanofiber films for visible-light-driven photocatalytic CO$_2$ reduction into CH$_4$, Adv. Mater. 34 (2022) 2200756.

[15] J. Zhang, J. Song, L. Liu, P. Zhang, Y. Si, S. Zhang, J. Yu, B. Ding, Electroconductive nanofibrous membranes with nanosheet-based microsphere-threaded heterostructures enabling oily wastewater remediation, J. Mater. Chem. A. 9 (2021) 15310–15320.

[16] J. Xu, X. Deng, Y. Dong, Z. Zhou, Y. Zhang, J. Yu, J. Cai, Y. Zhang, High-strength, transparent and superhydrophobic nanocellulose/nanochitin membranes fabricated via crosslinking of nanofibers and coating F-SiO$_2$ suspensions, Carbohydr. Polym. 247 (2020), 116694.

[17] R. Soni, T.-A. Asoh, H. Uyama, Cellulose nanofiber reinforced starch membrane with high mechanical strength and durability in water, Carbohydr. Polym. 238 (2020), 116203.

[18] S. Shi, R. Wu, S. Meng, G. Xiao, C. Ma, G. Yang, N. Wang, High-strength and anti-biofouling nanofiber membranes for enhanced uranium recovery from seawater and wastewater, J. Hazard. Mater. 436 (2022), 128983.

[19] P. Wu, Q. Luo, X. Zhang, J. He, C. Liu, W. Jiang, Universal rapid demulsification by vacuum suction using superamphiphilic and underliquid superamphiphobic polyurethane/diatomite composites, ACS Appl. Mater. Interfaces 14 (2022) 24775–24786.

[20] K. Wang, H. He, B. Wei, T.C. Zhang, H. Chang, Y. Li, X. Tian, Y. Fan, Y. Liang, S. Yuan, Multifunctional switchable nanocoated membranes for efficient integrated purification of oil/water emulsions, ACS Appl. Mater. Interfaces 13 (2021) 54315–54323.

[21] N. Gao, L. Wang, Y. Zhang, F. Liang, Y. Fan, Modified ceramic membrane with pH/ethanol induced switchable superwettability for antifouling separation of oil-in-acidic water emulsions, Sep. Purif. Technol. 293 (2022), 121022.

[22] Z. Chen, H.-Y. Xie, Y.-J. Li, G.-E. Chen, S.-J. Xu, Z.-L. Xu, Smart light responsive polypropylene membrane switching reversibly between hydrophobicity and hydrophilicity for oily water separation, J. Membr. Sci. 638 (2021), 119704.

[23] H.-R. Zhang, W.-X. Ma, X.-Y. Han, G.-E. Chen, Z.-L. Xu, Intelligent pH-responsive PMIA membrane with reversible wettability for controllable oil/water and emulsion separation, Appl. Surf. Sci. 615 (2023), 156392.

[24] T.F. Dehkordi, A.R. Shirin-Abadi, K. Karimipour, A.R. Mahdavian, CO$_2$-, electric potential-, and photo-switchable-hydrophilicity membrane (x-SHM) as an efficient color-changeable tool for oil/water separation, Polymer 212 (2021), 123250.

[25] P.D. Sutrisna, K.A. Kurnia, U.W.R. Siagian, S. Ismadji, I.G. Wenten, Membrane fouling and fouling mitigation in oil–water separation: a review, J. Environ. Chem. Eng. 10 (2022), 107532.

[26] H. Wang, J. Meng, F. Li, T. Li, Graphitic carbon nitride/ metal-organic framework composite functionalized cotton for efficient oil-water separation and dye degradation, J. Clean. Prod. 385 (2023), 135758.

[27] C. Meng, B. Ding, S. Zhang, L. Cui, K.K. Ostrikov, Z. Huang, B. Yang, J.H. Kim, Z. Zhang, Angstrom-confined catalytic water purification within Co-TiO$_x$ laminar membrane nanochannels, Nat. Commun. 13 (2022) 4010.

[28] Q.V. Ly, L. Cui, M.B. Asif, W. Khan, L.D. Nghiem, Y. Hwang, Z. Zhang, Membrane-based nanoconfined heterogeneous catalysis for water purification: A critical review, Water Res 230 (2023), 119577.

[29] Y. Zhao, Y. Gu, B. Liu, Y. Yan, C. Shan, J. Guo, S. Zhang, C.D. Vecitis, G. Gao, Pulsed hydraulic-pressure-responsive self-cleaning membrane, Nature 608 (2022) 69–73.

[30] Y.-X. Wang, Y.-J. Li, H. Yang, Z.-L. Xu, Super-wetting, photoactive TiO$_2$ coating on amino-silane modified PAN nanofiber membranes for high efficient oil-water emulsion separation application, J. Membr. Sci. 580 (2019) 40–48.

[31] T. Pan, Y. Liu, Z. Li, J. Fan, L. Wang, J. Liu, W. Shou, A Sm-doped Egeria-densa-like ZnO nanowires@PVDF nanofiber membrane for high-efficiency water clean, Sci. Total Environ. 737 (2020), 139818.

[32] J. Yang, J. Yu, J. Fan, D. Sun, W. Tang, X. Yang, Biotemplated preparation of CdS nanoparticles/bacterial cellulose hybrid nanofibers for photocatalysis application, J. Hazard. Mater. 189 (2011) 377–383.

[33] B. Sarkodie, J. Amesimeku, C. Frimpong, E.K. Howard, Q. Feng, Z. Xu, Photocatalytic degradation of dyes by novel electrospun nanofibers: A review, Chemosphere 313 (2023) 137654.

[34] K.Z. Qi, B. Cheng, J.G. Yu, W.K. Ho, Review on the improvement of the photocatalytic and antibacterial activities of ZnO, J. Alloy. Compd. 727 (2017) 792–820.

[35] S. Goktas, A. Goktas, A comparative study on recent progress in efficient ZnO based nanocomposite and heterojunction photocatalysts: A review, J. Alloy. Compd. 863 (2021), 158734.

[36] D. Lv, R.X. Wang, G.S. Tang, Z.P. Mou, J.D. Lei, J.Q. Han, S. De Smedt, R. H. Xiong, C.B. Huang, Ecofriendly electrospun membranes loaded with visible-light responding nanoparticles for multifunctional usages: highly efficient air filtration, dye scavenging, and bactericidal activity, ACS Appl. Mater. Interfaces 11 (2019) 12880–12889.

[37] T. Lu, Y. Deng, J. Cui, W. Cao, Q. Qu, Y. Wang, R. Xiong, W. Ma, J. Lei, C. Huang, Multifunctional applications of blow-spinning setaria viridis structured fibrous

membranes in water purification, ACS Appl. Mater. Interfaces 13 (2021) 22874–22883.

[38] Y. Zhang, J. Qiu, B. Zhu, M.V. Fedin, B. Cheng, J. Yu, L. Zhang, ZnO/COF S-scheme heterojunction for improved photocatalytic H_2O_2 production performance, Chem. Eng. J. 444 (2022), 136584.

[39] M. Nemiwal, T.C. Zhang, D. Kumar, Recent progress in g-C_3N_4, TiO_2 and ZnO based photocatalysts for dye degradation: Strategies to improve photocatalytic activity, Sci. Total Environ. 767 (2021), 144896.

[40] H.Z. Deng, X.G. Fei, Y. Yang, J.J. Fan, J.G. Yu, B. Cheng, L.Y. Zhang, S-scheme heterojunction based on p-type $ZnMn_2O_4$ and n-type ZnO with improved photocatalytic CO_2 reduction activity, Chem. Eng. J. 409 (2021), 127377.

[41] T. Garg, J. Renu, P. Kaur, Nitansh Kaur, V. Kumar, K. Tikoo, A. Kaushik, S. Singhal, An innovative Z-scheme g-C_3N_4/ZnO/$NiFe_2O_4$ heterostructure for the concomitant photocatalytic removal and real-time monitoring of noxious fluoroquinolones, Chem. Eng. J. 443 (2022), 136441.

[42] Y.M. Fu, Z.Q. Ren, J.Z. Wu, Y.Q. Li, W.L. Liu, P. Li, L.L. Xing, J. Ma, H. Wang, X. Y. Xue, Direct Z-scheme heterojunction of ZnO/MoS_2 nanoarrays realized by flowing-induced piezoelectric field for enhanced sunlight photocatalytic performances, Appl. Catal. B 285 (2021), 119785.

[43] L. Jiao, J. Wang, H.-L. Jiang, Microenvironment modulation in metal–organic framework-based catalysis, Acc. Mater. Res. 2 (2021) 327–339.

[44] G. Cai, P. Yan, L. Zhang, H.-C. Zhou, H.-L. Jiang, Metal–organic framework-based hierarchically porous materials: synthesis and applications, Chem. Rev. 121 (2021) 12278–12326.

[45] Z. Mo, D. Tai, H. Zhang, A. Shahab, A comprehensive review on the adsorption of heavy metals by zeolite imidazole framework (ZIF-8) based nanocomposite in water, Chem. Eng. J. 443 (2022), 136320.

[46] J. Wang, K. Shi, W. Liu, L. Yin, Y. Xu, D. Kong, L. Ni, Y. Yao, S. Li, Y. Zhang, S. Yang, H. He, Novel ZIF-8@CHs catalysts for photocatalytic degradation of tetracycline hydrochloride, Chem. Eng. J. 461 (2023), 142130.

[47] H.Y. Li, P. Mu, J. Li, Q.T. Wang, Inverse desert beetle-like ZIF-8/PAN composite nanofibrous membrane for highly efficient separation of oil-in-water emulsions, J. Mater. Chem. A 9 (2021) 4167–4175.

[48] W.J. Ma, Y.S. Li, M.J. Zhang, S.T. Gao, J.X. Cui, C.B. Huang, G.D. Fu, Biomimetic durable multifunctional self-cleaning nanofibrous membrane with outstanding oil/water separation, photodegradation of organic contaminants, and antibacterial performances, ACS Appl. Mater. Interfaces 12 (2020) 34999–35010.

[49] A. Xie, J. Cui, J. Yang, Y. Chen, J. Lang, C. Li, Y. Yan, J. Dai, Dual superlyophobic zeolitic imidazolate framework-8 modified membrane for controllable oil/water emulsion separation, Sep. Purif. Technol. 236 (2020), 116273.

[50] N. Chang, Y.-R. Chen, F. Xie, Y.-P. Liu, H.-T. Wang, Facile construction of Z-scheme AgCl/Ag-doped-ZIF-8 heterojunction with narrow band gaps for efficient visible-light photocatalysis, Colloids Surf. A 616 (2021), 126351.

[51] D. Tuncel, A.N. Okte, Improved adsorption capacity and photoactivity of ZnO-ZIF-8 nanocomposites, Catal. Today 361 (2021) 191–197.

[52] H. Piao, J. Zhao, M. Liu, S. Zhang, Q. Huang, Y. Liu, C. Xiao, Ultra-low power light driven lycopodium-like nanofiber membrane reinforced by PET braid tube with robust pollutants removal and regeneration capacity based on photo-Fenton catalysis, Chem. Eng. J. 450 (2022), 138204.

[53] F. Rombaldoni, K. Mahmood, A. Varesano, M. Bianchetto Songia, A. Aluigi, C. Vineis, G. Mazzuchetti, Adhesion enhancement of electrospun nanofiber mats to polypropylene nonwoven fabric by low-temperature oxygen plasma treatment, Surf. Coat. Technol. 216 (2013) 178–184.

[54] T. Cheng, S. Li, L. Xu, A. Ahmed, Controllable preparation and formation mechanism of nanofiber membranes with large pore sizes using a modified electrospinning, Mater. Des. 178 (2019), 107867.

[55] T. Pan, J. Liu, N. Deng, Z. Li, L. Wang, Z. Xia, J. Fan, Y. Liu, ZnO Nanowires@ PVDF nanofiber membrane with superhydrophobicity for enhanced anti-wetting and anti-scaling properties in membrane distillation, J. Membr. Sci. 621 (2021), 118877.

[56] P. Fakhri, B. Amini, R. Bagherzadeh, M. Kashfi, M. Latifi, N. Yavari, S. Asadi Kani, L. Kong, Flexible hybrid structure piezoelectric nanogenerator based on ZnO nanorod/PVDF nanofibers with improved output, RSC Adv. 9 (2019) 10117–10123.

[57] T. Yang, H. Pan, G. Tian, B. Zhang, D. Xiong, Y. Gao, C. Yan, X. Chu, N. Chen, S. Zhong, L. Zhang, W. Deng, W. Yang, Hierarchically structured PVDF/ZnO core-shell nanofibers for self-powered physiological monitoring electronics, Nano Energy 72 (2020), 104706.

[58] S. Zhang, J. Ding, D. Tian, R. Kang, X. Zhao, M. Chang, W. Yang, H. Xie, M. Lu, As (V) removal from aqueous environments using quaternary ammonium modified ZIF-8/chitosan composite adsorbent, Appl. Surf. Sci. 614 (2023), 156179.

[59] Z. Zhou, H. Zhu, S. Wu, Y. Lv, Y. Zheng, D. Chen, S. Zhu, Z. Li, Z. Cui, X. Liu, The combination of S-doped ZIF-8 with graphene oxide for enhanced near-infrared light photocatalytic and photothermal sterilization, Chem. Eng. J. 455 (2023), 140857.

[60] T.T. Bui, M.K. Shin, S.Y. Jee, D.X. Long, J. Hong, M.-G. Kim, Ferroelectric PVDF nanofiber membrane for high-efficiency PM0.3 air filtration with low air flow resistance, Colloids Surf., A 640 (2022), 128418.

[61] Y. Zeng, S. Liu, J. Xu, A. Zhang, Y. Song, L. Yang, A. Pu, Y. Ni, F. Chi, ZIF-8 in-situ growth on amidoximerized polyacrylonitrile beads for uranium sequestration in wastewater and seawater, J. Environ. Chem. Eng. 9 (2021), 106490.

[62] C. Shuai, X. Yuan, Y. Shuai, G. Qian, J. Yao, W. Xu, S. Peng, W. Yang, Nitrogen-doped carbon-ZnO heterojunction derived from ZIF-8: a photocatalytic antibacterial strategy for scaffold, Mater. Today Nano 18 (2022), 100210.

[63] J. Wang, Y. Xia, Y. Dong, R. Chen, L. Xiang, S. Komarneni, Defect-rich ZnO nanosheets of high surface area as an efficient visible-light photocatalyst, Appl. Catal. B. 192 (2016) 8–16.

[64] C. Wen, D. Li, J. Zhong, Z. Wang, S. Huang, H. Liu, J. Wu, P. Chen, W. Lv, G. Liu, In situ synthesis of S-scheme AgBr/BiOBr for efficient degradation of sulfonamide antibiotics: Synergistic effects of oxygen vacancies and heterojunctions promote exciton dissociation, Chem. Eng. J. 450 (2022), 138075.

[65] A. Xie, J. Cui, J. Yang, Y. Chen, J. Dai, J. Lang, C. Li, Y. Yan, Photo-Fenton self-cleaning membranes with robust flux recovery for an efficient oil/water emulsion separation, J. Mater. Chem. A. 7 (2019) 8491–8502.

[66] L. Zhang, Y. He, L. Ma, J. Chen, Y. Fan, S. Zhang, H. Shi, Z. Li, P. Luo, Hierarchically stabilized PAN/beta-FeOOH nanofibrous membrane for efficient water purification with excellent antifouling performance and robust solvent resistance, ACS Appl. Mater. Interfaces 11 (2019) 34487–34496.

[67] M. Järn, B. Granqvist, J. Lindfors, T. Kallio, J.B. Rosenholm, A critical evaluation of the binary and ternary solid–oil–water and solid–water–oil interaction, Adv. Colloid Interface Sci. 123–126 (2006) 137–149.

[68] M. Liu, S. Wang, Z. Wei, Y. Song, L. Jiang, Bioinspired design of a superoleophobic and low adhesive water/solid interface, Adv. Mater. 21 (2009) 665–669.

[69] T.S. Wong, S.H. Kang, S.K. Tang, E.J. Smythe, B.D. Hatton, A. Grinthal, J. Aizenberg, Bioinspired self-repairing slippery surfaces with pressure-stable omniphobicity, Nature 477 (2011) 443–447.

[70] Y. Wang, J. Di, L. Wang, X. Li, N. Wang, B. Wang, Y. Tian, L. Jiang, J. Yu, Infused-liquid-switchable porous nanofibrous membranes for multiphase liquid separation, Nat. Commun. 8 (2017) 575.

[71] X. Li, J. Liu, R. Qu, W. Zhang, Y. Liu, H. Zhai, Y. Wei, H. Hu, L. Feng, Universal and tunable liquid–liquid separation by nanoparticle-embedded gating membranes based on a self-defined interfacial parameter, Nat. Commun. 12 (2021) 80.

[72] Q. Wang, Y. Wang, B. Wang, Z. Liang, J. Di, J. Yu, Under-liquid dual superlyophobic nanofibrous polymer membranes achieved by coating thin-film composites: a design principle, Chem. Sci. 10 (2019) 6382–6389.

[73] X.J. Zeng, K.Q. Yang, C.Y. Huang, K. Yang, S.P. Xu, L. Wang, P.H. Pi, X.F. Wen, Novel pH-responsive smart fabric: from switchable wettability to controllable on-demand oil/water separation, ACS Sustain. Chem. Eng. 7 (2019) 368–376.

[74] N.W. Gao, L.C. Wang, Y. Zhang, F.J. Liang, Y.Q. Fan, Modified ceramic membrane with pH/ethanol induced switchable superwettability for antifouling separation of oil-in-acidic water emulsions, Sep. Purif. Technol. 293 (2022), 121022.

[75] T.W. Huo, F.R. Li, K.D. Jiang, W.T. Kong, X.Z. Zhao, Z. Hao, Y.L. Pan, Fluorocarbon-based selective-superwetting nanofibrous membranes with ultraviolet-driven switchable wettability for oil-water separation, ACS Appl. Mater. Interfaces 5 (2022) 13018–13026.

[76] G. Zhang, Z. Duan, Q.G. Wang, L. Li, W. Yao, C.H. Liu, Electrical potential induced switchable wettability of super-aligned carbon nanotube films, Appl. Surf. Sci. 427 (2018) 628–635.

[77] P. Zhang, S. Rajabzadeh, Q. Song, R.R. Gonzales, Y. Jia, S. Xiang, Z. Li, H. Matsuyama, Development of loose nanofiltration PVDF hollow fiber membrane for dye/salt separation, Desalination 549 (2023), 116315.

[78] J. Liu, Y. Chen, Y. Hu, Y. Zhang, G. Zhang, S. Wang, L. Zhang, A novel metal-organic framework-derived ZnO@ZIF-8 adsorbent with high efficiency for Pb (II) from solution: Performance and mechanisms, J. Mol. Liq. 356 (2022), 119057.

[79] J. Jiang, X. Wang, Y. Liu, Y. Ma, T. Li, Y. Lin, T. Xie, S. Dong, Photo-Fenton degradation of emerging pollutants over Fe-POM nanoparticle/porous and ultrathin g-C_3N_4 nanosheet with rich nitrogen defect: Degradation mechanism, pathways, and products toxicity assessment, Appl. Catal. B. 278 (2020), 119349.

[80] Y. Wang, L. Rao, P. Wang, Z. Shi, L. Zhang, Photocatalytic activity of N-TiO_2/O-doped N vacancy g-C_3N_4 and the intermediates toxicity evaluation under tetracycline hydrochloride and Cr(VI) coexistence environment, Appl. Catal. B. 262 (2020), 118308.

[81] T. Lu, F. Chen, Multiwfn: a multifunctional wavefunction analyzer, J. Comput. Chem. 33 (2012) 580–592.

[82] R.G. Parr, W. Yang, Density functional approach to the frontier-electron theory of chemical reactivity, J. Am. Chem. Soc. 106 (1984) 4049–4050.

[83] N. Jiang, X. Li, H. Guo, J. Li, K. Shang, N. Lu, Y. Wu, Plasma-assisted catalysis decomposition of BPA over graphene-CdS nanocomposites in pulsed gas-liquid hybrid discharge: Photocorrosion inhibition and synergistic mechanism analysis, Chem. Eng. J. 412 (2021), 128627.

[84] J. Li, H. Wang, N. Reddy, Z. Zhu, J. Zheng, W. Wang, B. Liu, C. Hu, MOFFeCo/B-CN composites achieve efficient degradation of antibiotics in a non-homogeneous concurrent photocatalytic-persulfate activation system, Sci. Total Environ. 858 (2023), 159795.

[85] N. Li, R. Li, X. Duan, B. Yan, W. Liu, Z. Cheng, G. Chen, La Hou, S. Wang, Correlation of active sites to generated reactive species and degradation routes of organics in peroxymonosulfate activation by co-loaded carbon, Environ. Sci. Technol. 55 (2021) 16163–16174.

[86] J. Guo, H. Sun, X. Yuan, L. Jiang, Z. Wu, H. Yu, N. Tang, M. Yu, M. Yan, J. Liang, Photocatalytic degradation of persistent organic pollutants by Co-Cl bond reinforced CoAl-LDH/$Bi_{12}O_{17}Cl_2$ photocatalyst: mechanism and application prospect evaluation, Water Res 219 (2022), 118558.

[87] N. Liu, N. Lu, H. Yu, S. Chen, X. Quan, Enhanced degradation of organic water pollutants by photocatalytic in-situ activation of sulfate based on Z-scheme g-C_3N_4/$BiPO_4$, Chem. Eng. J. 428 (2022), 132116.

[88] T. Lu, F. Chen, Bond Order Analysis Based on the Laplacian of Electron Density in Fuzzy Overlap Space, J. Phys. Chem. A 117 (2013) 3100–3108.

[89] J. Lin, Y. Hu, L. Wang, D. Liang, X. Ruan, S. Shao, M88/PS/Vis system for degradation of bisphenol A: Environmental factors, degradation pathways, and toxicity evaluation, Chem. Eng. J. 382 (2020), 122931.

[90] R.A. Torres-Palma, J.I. Nieto, E. Combet, C. Pétrier, C. Pulgarin, An innovative ultrasound, Fe^{2+} and TiO_2 photoassisted process for bisphenol a mineralization, Water Res 44 (2010) 2245–2252.

[91] S. Zuo, D. Li, Z. Guan, F. Yang, J. Song, H. Xu, D. Xia, H. Li, X. Li, A directional Built-in electric field mediates the electron transfer synergy mechanism of the Radical/Nonradical pathway in FeOCl-CuO, Chem. Eng. J. 430 (2022), 133004.

[92] M. Li, D. Li, Z. Guan, Q. Xu, Y. Shi, D. Xia, Carboxy-functionalized sludge-derived biochar for efficiently activating peroxymonosulfate to degrade bisphenol A, Sep. Purif. Technol. 297 (2022), 121525.

[93] L. Zhang, N. Yang, Y. Han, X. Wang, S. Liu, L. Zhang, Y. Sun, B. Jiang, Development of polyacrylonitrile/perovskite catalytic membrane with abundant channel-assisted reaction sites for organic pollutant removal, Chem. Eng. J. 437 (2022), 135163.

[94] J.-S. Wang, X.-H. Yi, X. Xu, H. Ji, A.M. Alanazi, C.-C. Wang, C. Zhao, Y.V. Kaneti, P. Wang, W. Liu, Y. Yamauchi, Eliminating tetracycline antibiotics matrix via photoactivated sulfate radical-based advanced oxidation process over the immobilized MIL-88A: Batch and continuous experiments, Chem. Eng. J. 431 (2022), 133213.

[95] Q. Su, J. Li, H. Yuan, B. Wang, Y. Wang, Y. Li, Y. Xing, Visible-light-driven photocatalytic degradation of ofloxacin by g-C_3N_4/NH_2-MIL-88B(Fe) heterostructure: Mechanisms, DFT calculation, degradation pathway and toxicity evolution, Chem. Eng. J. 427 (2022), 131594.

[96] P. Xu, P. Wang, X. Li, R. Wei, X. Wang, C. Yang, T. Shen, T. Zheng, G. Zhang, Efficient peroxymonosulfate activation by CuO-Fe_2O_3/MXene composite for atrazine degradation: Performance, coexisting matter influence and mechanism, Chem. Eng. J. 440 (2022), 135863.

[97] M. Wang, Q. Gao, M. Zhang, M. Zhang, Y. Zhang, J. Hu, G. Wu, In-situ formation of durable akaganeite (beta-FeOOH) nanorods on sulfonate-modified poly (ethylene terephthalate) fabric for dual-functional wastewater treatment, J. Hazard. Mater. 386 (2020), 121647.

[98] H. Sepehrmansourie, H. Alamgholiloo, N. Noroozi Pesyan, M.A. Zolfigol, A MOF-on-MOF strategy to construct double Z-scheme heterojunction for high-performance photocatalytic degradation, Appl. Catal. B. 321 (2023), 122082.

[99] Y. Wang, C. Yang, Y. Zhang, L. Guo, Y. Wang, G. Gao, F. Fu, B. Xu, D. Wang, Nanoarchitectonics of CdS/$ZnSnO_3$ heterostructures for Z-Scheme mediated directional transfer of photo-generated charges with enhanced photocatalytic performance, Int. J. Hydrog. Energy 47 (2022) 9566–9578.

[100] H. Dai, X.Z. Yuan, L.B. Jiang, H. Wang, J. Zhang, J.J. Zhang, T. Xiong, Recent advances on ZIF-8 composites for adsorption and photocatalytic wastewater pollutant removal: Fabrication, applications and perspective, Coord. Chem. Rev. 441 (2021), 213985.

[101] M.H. Chen, Q.Y. Lu, Y.M. Li, M.M. Chu, X.B. Cao, ZnO@ZIF-8 core-shell heterostructures with improved photocatalytic activity, CrystEngComm 23 (2021) 4327–4335.

[102] L. Chen, J.T. Ren, Z.Y. Yuan, Enabling Internal Electric Fields to Enhance Energy and Environmental Catalysis, Adv. Energy Mater. 13 (2023) 2203720.

[103] H. Piao, J. Zhao, S. Zhang, Q. Quan, J. Hu, Q. Huang, R. Zhu, L. Fan, C. Xiao, Polypyrrole/cadmium sulfide/nickel hollow fiber as an enhanced and recyclable intrinsic photocatalyst for pollutant removal and high-effective hydrogen evolution, Int. J. Hydrog. Energy (2022).

[104] S. Zheng, H. Chen, X. Tong, Z. Wang, J.C. Crittenden, M. Huang, Integration of a photo-Fenton reaction and a membrane filtration using CS/PAN@ FeOOH/g-C_3N_4 electrospun nanofibers: synthesis, characterization, self-cleaning performance and mechanism, Appl. Catal. B. 281 (2021), 119519.

[105] W. Lu, C. Duan, C. Liu, Y. Zhang, X. Meng, L. Dai, W. Wang, H. Yu, Y. Ni, A self-cleaning and photocatalytic cellulose-fiber- supported "Ag@AgCl@MOF-cloth'' membrane for complex wastewater remediation, Carbohydr. Polym. 247 (2020), 116691.

[106] W.-J. Pan, C. Xiong, Q.-P. Wu, J.-X. Liu, H.-M. Liao, W. Chen, Y.-S. Liu, L. Zheng, Effect of BPA on the germination, root development, seedling growth and leaf differentiation under different light conditions in Arabidopsis thaliana, Chemosphere 93 (2013) 2585–2592.

[107] C. Xiao, L. Wang, Q. Zhou, X. Huang, Hazards of bisphenol A (BPA) exposure: a systematic review of plant toxicology studies, J. Hazard. Mater. 384 (2020), 121488.